JACS
JOURNAL OF THE AMERICAN CHEMICAL SOCIETY
Article
pubs.acs.org/JACS

Cation Size Mismatch and Charge Interactions Drive Dopant Segregation at the Surfaces of Manganite Perovskites

Wonyoung Lee,† Jeong Woo Han,† Yan Chen, Zhuhua Cai, and Bilge Yildiz*

Laboratory for Electrochemical Interfaces, Department of Nuclear Science and Engineering, Massachusetts Institute of Technology, 77 Massachusetts Avenue, Cambridge, Massachusetts 02139, United States

Supporting Information

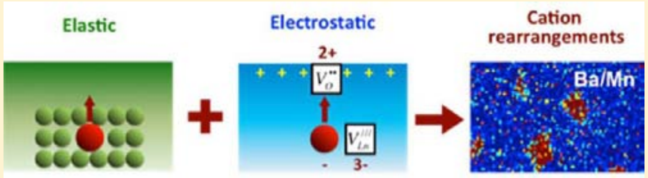

ABSTRACT: Cation segregation on perovskite oxide surfaces affects vastly the oxygen reduction activity and stability of solid oxide fuel cell (SOFC) cathodes. A unified theory that explains the physical origins of this phenomenon is therefore needed for designing cathode materials with optimal surface chemistry. We quantitatively assessed the elastic and electrostatic interactions of the dopant with the surrounding lattice as the key driving forces for segregation on model perovskite compounds, $LnMnO_3$ (host cation Ln = La, Sm). Our approach combines surface chemical analysis with X-ray photoelectron and Auger electron spectroscopy on model dense thin films and computational analysis with density functional theory (DFT) calculations and analytical models. Elastic energy differences were systematically induced in the system by varying the radius of the selected dopants (Ca, Sr, Ba) with respect to the host cations (La, Sm) while retaining the same charge state. Electrostatic energy differences were introduced by varying the distribution of charged oxygen and cation vacancies in our models. Varying the oxygen chemical potential in our experiments induced changes in both the elastic energy and electrostatic interactions. Our results quantitatively demonstrate that the mechanism of dopant segregation on perovskite oxides includes both the elastic and electrostatic energy contributions. A smaller size mismatch between the host and dopant cations and a chemically expanded lattice were found to reduce the segregation level of the dopant and to enable more stable cathode surfaces. Ca-doped $LaMnO_3$ was found to have the most stable surface composition with the least cation segregation among the compositions surveyed. The diffusion kinetics of the larger dopants, Ba and Sr, was found to be slower and can kinetically trap the segregation at reduced temperatures despite the larger elastic energy driving force. Lastly, scanning probe image contrast showed that the surface chemical heterogeneities made of dopant oxides upon segregation were electronically insulating. The consistency between the results obtained from experiments, DFT calculations, and analytical theory in this work provides a predictive capability to tailor the cathode surface compositions for high-performance SOFCs.

1. INTRODUCTION

Cation segregation at the surface and the interfaces of transition-metal oxides impacts the reactions that are often critical to the overall device performance in a range of device applications, including solid oxide fuel cells,[1−9] oxygen permeation membranes,[10,11] batteries,[12−15] and magnetic,[16−19] catalytic,[20,21] and ferroelectric[22,23] materials. In particular, cation segregation on perovskite oxide surfaces impacts tremendously the reactivity and stability of solid oxide fuel cell (SOFC) cathodes.[1,3,4,6−8,24,25] The slow rate of oxygen reduction reaction (ORR), which is generally agreed to be limited by the surface exchange reactions on mixed ionic electronic conducting cathodes,[26,27] imposes the main barrier for implementation of high-performance SOFCs at intermediate temperatures (500−700 °C).[28,29] To attain highly reactive and stable cathode surfaces for fast ORR kinetics, it is important to tailor the catalytic activity of transition-metal oxide cathode with a thorough knowledge of the surface composition and structure at the atomic level. The surface of the SOFC cathodes, typically made from perovskite-related oxides, is not static, and the structure and chemistry are driven dynamically by the surrounding environments at elevated temperatures, in oxygen partial pressure, and under electrochemical potentials. The complexity of these surfaces and the harsh environments that they function in have prohibited thus far the development of clear fundamental principles that relate their surface state to the ORR kinetics. This is important not only for the reactivity but also for the durability of the electrodes.

Cation segregation at the surface of perovskite oxides has been a commonly observed phenomenon that has direct relations to cathode reactivity and stability in ORR.[5,30−33] An example is the Sr enrichment at the surface of $La_{1-x}Sr_xMnO_3$ (LSM) and $La_{1-x}Sr_xCoO_3$ (LSC) that are widely studied cathodes. Upon dopant segregation, the surface can exist in different chemical phases, including the perovskite-termination structure with the Sr replacing La on the A-site at the surface[30,31] and phase separation in the form of Ruddlesden−Popper (RP) phases[32] or dopant-oxides (e.g., SrO).[1,5,34] At the surface of LSM, the concentration of Sr dopant was shown to increase with decreasing oxygen pressure[31] and increasing

Received: December 22, 2012
Published: May 3, 2013

temperature (>500 °C).[33] On another well-studied perovskite, $SrTiO_3$ (STO), the surface was drastically altered by formation of Sr-rich RP phases in oxidizing conditions and Ti-rich phases in reducing conditions.[35] Furthermore, such surface segregates of secondary phases can form a spatially heterogeneous surface chemistry and structure, as found on LSC[1] in our previous work and on STO.[36] Each surface structure formed upon cation segregation is associated with different ORR reactivity. A unified theory that explains the physical origins of dopant segregation on perovskite-related oxides is therefore needed for designing cathode materials with optimal surface chemistry for fast and stable ORR kinetics.

Thermodynamic and kinetic conditions that drive surface segregation and transitions between possible surface phases/structures on perovskite oxides have not been well explored and explained. The different surface free energies (surface bond breaking) and the different atomic sizes (lattice strain) of the elements cause surface segregation to reduce the free energy of the system.[19,37−41] Especially, on metal oxides of ionic nature, the existence of a space-charge layer near the surface also provides a strong chemical potential to drive segregation.[42−46] Therefore, it is reasonable to say that the key driving forces to segregation originate from the elastic and electrostatic interactions of the dopant with the surrounding lattice in a perovskite oxide. The specific mechanisms that manifest these interactions are related to the size mismatch between the dopant and host cations and the associated elastic energy minimization by pushing the larger or smaller dopant to free surfaces or interfaces[18,19,38,47] and to the charged defect interactions, such as a strong association of dopant cations with oxygen vacancies, which can drive the dopants to positively charged interfaces where oxygen vacancies are in abundance[44] as well as with polar surfaces. We provide this description of the contributors to dopant segregation in analogy to the vacancy-dopant association energy in bulk oxides. Vacancy-dopant association generally contains two terms: the elastic interactions arising from the size mismatch of dopants with host cations and the Coulombic term which reflects the electrostatic attraction between the constituents.[48]

Recently, Harrison has hypothesized that the surface charging on the $(La,Sr)MnO_3$ is the origin of the segregation of Sr at the surface of LSM.[49] On the (100) surface of $La_xSr_{1-x}MnO_3$, AO planes with a uniform distribution of Sr and La cations take a charge of $+e(1 - x)$ per A-site. Terminating such a set of charged planes leaves an effective surface charge of $\pm e(1 - x)/2$ per A-site. Harrison's work constructed an electrostatic model of the interaction of Sr with the charged surfaces on LSM. With this model, it was shown that the large energy associated with a charged surface could be minimized by depleting the La and increasing the Sr concentration at and near the surface of LSM. This result would seem to give compelling evidence that the surface charging is a source of the segregation of the dopant at the surface of LSM. On the other hand, only this electrostatic contribution alone cannot provide an accurate quantitative prediction of the large extents of segregation on such materials as acknowledged in the same work[49] and as also shown in our results later in this paper. Past work on titanates have suggested the importance of both the elastic and electrostatic interactions in determining cation segregation on the surface.[50] However, the analysis remained at a phenomenological level, and the electrostatic interaction was considered to be based on only the effects of surface adsorbates. An alternative model that can be discussed is the kinetic demixing phenomenon when the material is subjected to an oxygen chemical potential gradient across.[51] However, significant cation segregation is found on many perovskite surfaces even without the presence of a gradient of oxygen chemical potential, therefore, we believe this model cannot explain the intrinsic drivers to cation segregation.

In this paper, we quantitatively assessed the electrostatic and elastic energy minimization as two main driving forces of dopant segregation at the surface of manganite-based perovskite oxides, $LnMnO_3$. The host cation Ln = La was used in our experiments, and Ln = La and Sm were used in our computational work as the model material systems. We probed the surface chemistry and structure with X-ray photoelectron (XPS) and Auger electron spectroscopy (AES) on model dense thin films. The effects of the elastic energy on the cation segregation were investigated by varying the size mismatch between the dopant (Ca, Sr, Ba) and host cation in the perovskite thin films. The effects of the electrostatic energy on the cation rearrangements were investigated with control of the oxygen chemical potential during the annealing of thin films and with control of the distribution of charged defects in our models. Density functional theory (DFT) calculations and analytical models were used to elucidate the underlying physics of cation segregation, including the kinetic effects, and to quantitatively decouple the contribution of the elastic and electrostatic energy to segregation. We show, using image-contrast between atomic force microscopy (AFM) and scanning tunneling microscopy (STM), that the surface chemical heterogeneities upon dopant segregation were electronically insulating, and thus, they are expected to hinder the ORR kinetics. Our results demonstrate that the mechanism of dopant segregation on perovskite oxides includes important contributions from both the elastic and the electrostatic energy—a smaller size mismatch between the dopant and host cations, a chemically expanded lattice, and reduction of the surface positive charge can reduce the segregation level of the A-site dopant and enable more stable cathode surfaces.

2. APPROACH

We hypothesized that the elastic and electrostatic interactions are the key driving forces of cation segregation on perovskite oxide surfaces. To quantitatively assess these two contributions, we experimentally determined the chemical composition and structures of dopant-enriched surfaces of the $LaMnO_3$ films upon annealing at elevated temperatures in varying oxygen pressures. We interpreted our experimental results quantitatively and predictively using DFT calculations and analytical models. The parameters that affect the magnitude of the two driving forces were varied in our experiments and computational models; in particular, the dopant size, the lattice parameter, and the distribution of charged vacancies.

We note that our DFT calculations focused on the dopant segregation within the perovskite-terminated surface lattice by simply replacing the host cation with the dopant, while our experiments showed ultimately heterogeneous phase separation at the surface. Enrichment of the dopant on the A-site sublattice at the surface would lead to a larger concentration of the dopant at the surface compared to the bulk nominal level. If the concentration of the segregated dopants increases beyond the solubility limit at the perovskite surface at elevated temperatures, phase-separated particles, such as $SrO/Sr(OH)_2$, or layered RP phases can form.[1,32] The calculated total segregation energy on the perovskite lattice is a quantitative measure of the increase in the concentration of dopant cations on the perovskite surface. This quantity at the same time indicates the extent of the new phase formation because the secondary phases will form only following the increase in dopant cation concentration beyond the solubility limit at the surface. Therefore, our computational approach here is applicable in assessing the "tendency" to restructure or phase-separate because of dopant segregation at the surface, even if the possible secondary phases are not explicitly captured in our models. The following subsections describe the method details in our approach.

2.1. Experimental Methods. *2.1.1. Thin Film Fabrication.* In the experimental part of our investigation, epitaxial dense thin films of $La_{0.8}D_{0.2}MnO_3$ (D = Ca, Sr, Ba) with the same crystallographic orientation were used as a model system. The use of such thin film model systems enabled us to eliminate the effects of a complex microstructure on the segregation process and to focus on the key parameters that we controlled for varying the extent of elastic and electrostatic energy as the drivers to segregation. Three sets of dense thin films were fabricated with the three different dopants, $La_{0.8}Ca_{0.2}MnO_3$ (LCM), $La_{0.8}Sr_{0.2}MnO_3$ (LSM), and $La_{0.8}Ba_{0.2}MnO_3$ (LBM). We chose Ca, Sr, and Ba as the dopants because they have the same formal charge of +2 but different ionic radii, as shown in the Table 1. By varying only the size of the dopant cations but not their charge, we systematically induced the elastic energy differences in the system while maintaining the same electrostatic interactions of the dopant. The largest size mismatch between the dopant and host cations on the A-site was in the LBM film, followed by LSM and LCM. In our computational work, we further extended the results to doped $SmMnO_3$, where a larger mismatch between the host and these dopants prevailed compared to the $LaMnO_3$ system.

Table 1. Size Mismatch, Denoted as $(R_{dopant} - R_{host})/R_{host}$ (%), between the Dopant and Host Cations in $LaMnO_3$ and $SmMnO_3$[a]

	dopant cation		
host cation	Ca^{2+}	Sr^{2+}	Ba^{2+}
La^{3+}	−1.5	+5.9	+18.4
Sm^{3+}	+8.1	+16.1	+29.8

[a] Shannon's ionic radii[52] are used as the cation radii, *R*.

Constituent powders were prepared by a modified Pechini or polymer precursor synthesis method.[53] High purity $La(NO_3)_3·6H_2O$ (99.9% purity), $Ca(NO_3)_2·4H_2O$ (99.98% purity), $Sr(NO_3)_2$ (99.97% purity), $Ba(NO_3)_2$ (99.999% purity), and $Mn(NO_3)_2·4H_2O$ (99.98% purity) (all precursors from Alfa Aesar) were dissolved at the stoichiometric ratio in distilled water with citric acid. Ethylene glycol was then added, and the solution was heated until self-combustion occurred. The as-synthesized powders were subsequently calcined at 1100 °C for 6 h in air with ramping rate of 3 °C/min. The powders were ground in an agate mortar and pestle and were uniaxially pressed to produce 1 in. diameter target. The target was sintered at 1300 °C in air for 20 h with ramping rate of 3 °C/min. All films with a thickness of about 20 nm were deposited on single-crystal $SrTiO_3$ (STO) (100) substrates using pulsed laser deposition (PLD). Highly epitaxial films of (100) orientation were obtained in all three sets of compositions to avoid microstructural effects on the segregation behavior. PLD was performed with a KrF excimer laser at a wavelength of 248 nm and laser beam energy of 550 mJ/pulse at 10 Hz, at 815 °C with an oxygen pressure of 10 mTorr and with the target-to-substrate distance of 6 cm. After deposition, the sample was cooled at 10 °C/min to room temperature in an oxygen pressure of 10 Torr.[30]

2.1.2. Thin Film Characterization. A Veeco/Digital Instrument Nanoscope IV was used to perform tapping mode AFM for characterizing the surface morphology.

A Physical Electronics Model 700 Auger electron spectroscopy (AES) was used to identify the surface cation content, with the ability to detect lateral heterogeneities in cation compositions with high spatial resolution at the nm-scale. Incident electrons of 25 keV and 10 nA were used for both SEM imaging and the Auger electron excitation. The Ba MNN, Sr LMM, La MNN, and Mn LMM Auger emissions were measured for quantifying the surface cation composition using peak-to-peak intensities of the tight scans. The sampling depths of these AES electrons are ~4.0 nm for Ba MNN, ~8.5 nm for Sr LMM, ~4.0 nm for La MNN, and ~4.0 nm for Mn LMM.[54]

Angle-resolved X-ray photoelectron spectroscopy (AR-XPS) was used to identify the cation chemistries with near-surface depth resolution on thin films. The Omicron EA 125 hemispherical analyzer and Omicron DAR 400 Mg/Al dual anode nonmonochromated X-ray source were used with Mg Kα X-ray (1253.6 eV) operated at 300 W. CasaXPS 2.3.15 software was used for spectral analysis and compositional quantification. While most samples were examined in their as-annealed conditions, the as-deposited samples were examined after removing carbon contamination from their surfaces prior to the analysis. This was done by heating the samples in an oxygen pressure of 5×10^{-5} mbar at 500 °C for 1.5 h in the UHV chamber.[1] Spectra were acquired with emission angles from 0° to 80° as defined relative to the surface normal. For the excitation energy of 1253.6 eV, the sampling depths of these photoelectrons at normal emission are ~6.5 nm for Sr 3d, Ba 4d, and La 4d, ~5.5 nm for Ca 2p, and ~4.0 nm for Mn 2p.[54] At the emission angle of 80°, the sampling depth of each element are ~20% of those at the emission angle of 0°, making the measurements significantly more surface sensitive.

Although the high surface sensitivity obtained by AR-XPS provides a unique benefit to explore the extreme surface properties, it also results in incomplete information about the actual amount of segregated dopants when there are significant chemical and structural heterogeneities at the surface upon segregation. As we present in the Results and Discussion, dopant segregation after annealing resulted in the formation of particles that were clustered at the surface with 20−400 nm in width and 2−40 nm in height. Because the segregate particles were much higher than the penetration depth of the AR-XPS analysis, an apparent decrease of dopant cation content was found from the AR-XPS quantification upon annealing, while the spatially resolved AES showed a clear and significant enrichment of dopant cations (Ba and Sr in particular) at the surface. To compensate for this geometry-related artifact and to more accurately obtain the amount (extent) of dopant enrichment upon annealing, we combined the calculated the cation composition from AR-XPS and the geometric information from AFM. The procedure is described in Supporting Information. All cation spectra acquired with two emission angles were used to calculate the relative cation intensity ratios after two sequential normalization procedures. First, cation intensity ratios obtained from two emission angles were normalized by dividing cation intensity ratio at the emission angle of 80° by that at the emission angle of 0°; e.g., $[\mathrm{Ba/Mn}]_{\theta=80^\circ}/[\mathrm{Ba/Mn}]_{\theta=0^\circ}$ in case of the LBM films. By dividing cation intensity ratios obtained, we minimized the possible quantification errors, which arose from the different attenuation depths of different binding energies of cations. Second, all cation intensity ratios were presented with respect to the as-deposited samples to compare the relative changes in each cation composition as a function of temperature. This ratio then provides the measure of dopant segregation at the surface as a function of annealing. This series of normalization procedures allows a direct comparison of the surface segregation among the three sets of thin films.

STM was employed to investigate the surface morphology and electronic structure on the thin films. The measurements were performed in a modified UHV system (VT-STM, Omicron Nanotechnology). Data were acquired in the constant-current mode using etched Pt/Ir tips, with a sample bias voltage of 1−2 V and a tunneling current of 10−50 pA. The measurements were performed after sample cleaning at 500 °C for 1.5 h in $\sim 3 \times 10^{-3}$ mbar of oxygen. The sample was then cooled down to room temperature slowly in the same oxygen pressure.

Ex situ X-ray diffraction (XRD) $2\theta-\omega$ scans were performed to determine the crystal structure, the phase purity, and the strain states of the thin films. The measurements employed a high-resolution four-circle Bruker D8 Discover diffractometer, equipped with a Göbel mirror, four-bounce Ge(022) channel-cut monochromator, Eulerian cradle, and a scintillation counter, using Cu Kα1 radiation.

2.1.3. Annealing Conditions. The samples were annealed in different oxygen pressures as a function of temperature. Samples annealed in air were subjected to a heating ramp rate of 10 °C/min and maintained at the set temperature for 1 h in a tube furnace. After annealing at the desired temperature for 1 h, the samples were cooled down to ~300 °C with a cooling ramp rate of 20 °C/min. The samples were then directly transferred to the UHV chamber for subsequent XPS analysis, preserving the surface states at elevated temperature and minimizing the possible surface contamination. Separate sets of samples were annealed for 1 h at each temperature in lower oxygen pressures in the UHV chamber with the base pressure of $\sim 1 \times 10^{-6}$ mbar and $\sim 1 \times 10^{-9}$ mbar. The XPS and AES measurements were performed in $\sim 1 \times 10^{-9}$ mbar for all samples. XPS measurements on samples annealed in $\sim 1 \times 10^{-9}$ mbar were performed *in situ* at high temperature. All other measurements were performed upon cooling the samples.

2.2. Computational Methods and Models. Similarly to the experimental model systems, the elastic energy differences were introduced by varying the dopant size with respect to the host cation while keeping the same charge state. $\mathrm{LaMnO_3}$ and $\mathrm{SmMnO_3}$ were used as the host lattice and Ca, Sr, and Ba as the dopants (see Table 1). Electrostatic energy differences were introduced by constructing seven different models with varying distribution of charged oxygen vacancies and A-site cation vacancies.

2.2.1. DFT Calculations. We performed plane wave DFT calculations using the Vienna *ab initio* simulation package (VASP).[55] We employed the generalized gradient approximation (GGA) parametrized by Perdew and Wang[56] along with the projector augmented wave (PAW) method[57] to describe the ionic cores. To avoid the self-interaction errors that occur in the traditional DFT for strongly correlated electronic systems, we employed the DFT+U method within Dudarev's approach[58] accounting for the on-site Coulomb interaction in the localized d orbitals, with an effective U-J = 4 eV.[30,59,60] All calculations used a plane wave expansion cutoff of 400 eV and included spin polarization. Geometries were relaxed using a conjugate gradient algorithm until the forces on all unconstrained atoms were <0.03 eV/Å. The description of the surface segregation energy calculation is presented in the Supporting Information, and the same approach was reported in our recent work on LSM.[30]

2.2.2. Analytical Models. Our DFT calculations for segregation energy, E_{segr}, as described in Supporting Information, can only provide the total energetics upon dopant segregation in the system. To quantitatively decouple each contribution and to investigate if indeed E_{segr} can be described as the sum of elastic energy, E_{elastic}, and electrostatic energy, $E_{\mathrm{electrostatic}}$, we calculated each of the two interaction energies from conventional analytical models. By this analysis, the relative importance of the elastic and electrostatic interactions to the segregation can also be evaluated.

2.2.2.1. Elastic Energy. One of the main driving forces of dopant segregation in solid solutions is the relaxation of the strain energy generated around dopant cations with sizes larger or smaller than the host cation. An analytic model for the elastic energy of a misfitting solute was proposed by Friedel[61] and used here to calculate the elastic energy of dopants in the perovskite Manganite oxides.

$$E_{\mathrm{elastic}} = \frac{24\pi G K r_a r_b (r_a - r_b)^2}{3K r_a + 4G r_b} \tag{1}$$

where K is the bulk modulus of the solute, G is the shear modulus of the solvent, and r_a and r_b are the cation radii of the solute and solvent species, respectively. The equation was deduced from the continuous linear elasticity for the elastic energy released when an odd-sized atom is transferred from the bulk onto the strain-free surface of the alloy. It was originally developed for metal solid solutions,[61] but has also been used to predict an elastic strain energy contribution to the enthalpy of segregation for oxide solutions.[39−41] Eq 1 has the advantage of simplicity to estimate the elastic energy, but it has some limitations. First, it can only be applicable to dilute solutions. Second, the lattice strain due to the size mismatch should be fully relaxed when a larger dopant segregates to the surface.

To systematically induce elastic energy differences in our computational model, we varied the radius of selected dopant cations with respect to the host cation on the A-site as shown in Table 1. In eq 1, we used Shannon's ionic radii[52] that describes the physical size of ions in a solid, considering the coordination number and spin state. Among the pairs of dopants and hosts we examined, Ba dopant in $\mathrm{SmMnO_3}$ has the maximum size difference, +29.8%, while Ca dopant in $\mathrm{LaMnO_3}$ has the minimum size difference, −1.5%. As shown in Table S1, the bulk (shear) modulus for each dopant (host) was calculated in a bulk molecular unit, $\mathrm{AMnO_3}$ (A = La, Sm, Ca, Sr, and Ba), using DFT. For the modulus calculations, we employed the stress−strain approach[62] to directly calculate the stress tensor. Once the stress tensor components were computed, the elastic constants matrix was derived, from which we obtained the bulk and shear moduli.

2.2.2.2. Electrostatic Energy. The charge interactions between the dopants, the oxygen and cation vacancies, and the polar surfaces were considered as another important driving force to cation segregation on the perovskite oxides. Here first we justify how oxygen vacancies at the surface can contribute to the electrostatic attraction of the A-site dopants to the surface, based on the presence of a positively charged surface and a space charge zone. Formation energy of oxygen vacancies is typically smaller at the surface compared to the bulk of oxides, including that on the $LaMnO_3$.[63−65] For example, approximately 10^6 times higher vacancy concentration at the surface than in the bulk was predicted for $La_{0.9}Sr_{0.1}MnO_3$ under typical SOFC operating conditions of $pO_2 = 1$ atm and 1173 K.[6] In the doped manganites, formation of oxygen vacancies (that are positively charged) upon reduction of the material is associated with electron release into the material. If electrons are localized on the transition metal (Mn in $LaMnO_3$), then they significantly contribute to electrostatic interactions. By performing Bader charge analysis upon DFT calculations, we confirmed that in our models, electrons localize at the Mn cation upon creation of an oxygen vacancy, as expected. If the created oxygen vacancies and localized electrons stay together at the surface layer, making an electroneutral surface, they would contribute no net electrostatic attraction to charged dopant defects. However, an increase of oxygen vacancies at the surface layer makes a “positively charged surface” on the mixed ionic electronic conducting (MIEC) oxides,[27] similar to those studied in our calculations. Such positively charged surface is then accompanied by a decrease of oxygen vacancy concentration and an increase of electrons beneath the surface in the diffuse space charge layer (associated with a positive space charge potential).[27,66,67] This configuration of a “positive surface”, and “the electrons (negative) being more in the space charge zone beneath the surface”, would further contribute to the electrostatic attraction of the negatively charged dopant defect (Ca^{2+}, Sr^{2+}, Ba^{2+} on the La^{3+}-site) to the surface and its repulsion from beneath the surface. Consequently, under all conditions where the surface is positively charged and accompanied by electrons localized in the space charge layer beneath the surface, the MIEC surface would electrostatically attract the negatively charged dopant defects. The spatial extent and strength of the space charge zone depends on the material, e.g., more extensive on $SrTiO_3$ compared to that on heavily doped manganites whose Debye screening length (∼1 nm)[68] is shorter than that of $SrTiO_3$.

All dopants used here, Ca, Sr, and Ba have a formal charge of +2, while the hosts have +3 charge. The oxygen vacancies have a formal charge of +2, and the A-site (Ln) cation vacancies have −3 charge state.[49,69] Assuming that $LnMnO_3$ is purely ionic, we calculated electrostatic energy by Coulomb’s law as below:

$$E_{\text{electrostatic}} = \sum -\frac{Q_1 Q_2}{4\pi\varepsilon R_{12}} \tag{2}$$

where Q_1 and Q_2 are two charges separated by a distant R_{12} in a medium of dielectric constant ε. We took $\varepsilon_0 = 56.17\varepsilon_0$ caculated by Islam et al.[70,71] as a static dielectric constant of $LnMnO_3$, where ε_0 is the vacuum permittivity. From this equation, it is expected that a surface oxygen vacancy of formal charge +2 attracts the dopant that substituted the host (this complex has a formal charge of −1), driving the dopant toward the surface on the host sublattice. We considered the sum of the charge interactions between a dopant and all the ions (La, dopant, Mn, and O) within the separation distance between the two charged defects we modeled in Figure 2, not just the interaction between the two point charge defects at the surface and in the bulk. This approach then resembles the generalized Born (GB) method,[72] taking into account at least partially the screening imposed by other atoms than the two point charges. A more accurate GB method could be used here to improve the precision of the calculated electrostatic energy contribution to the total segregation energy.

The DFT models used in our simulations are limited in size (an inherent limitation of DFT beyond our work), and thus, we cannot capture explicitly the space charge zone described above. Instead, we impart the electrostatic energy differences by varying the distribution of oxygen and A-site cation vacancies in the DFT model (Figure 1). In this way, we also generalize the role of electrostatic interactions in cation segregation regardless of the strength of space charge in a given composition. Seven models were constructed with different configurations of oxygen and cation vacancies through the thin film models. While at the low oxygen pressure, the concentration of oxygen vacancies dominates, and in the high oxygen pressure range, A-site cation vacancies are expected to be dominant over the oxygen vacancies in these compounds.[73,74] Furthermore, A-site deficient perovskites were often intentionally synthesized to attain better interface stability and performance.[75−77] In Figure 1, the models are listed in the order of increasing attractive interaction to the dopant at the surface. For example, in model 1, a surface cation vacancy (of charge −3) repels the dopant on the A-site (of charge −1) from the surface. In addition, an oxygen vacancy (of charge +2) near the dopant in the bulk attracts the dopant. As a result, the dopant prefers to remain in the bulk. On the other hand, in model 7, a surface oxygen vacancy attracts the dopant. Simultaneously, a cation vacancy near the dopant in the bulk prefers the host cation relative to the dopant cation. Therefore, segregation of the dopant to the surface is very favorable due to the combination of the attractive interaction toward the surface and the repulsive interaction from the bulk. Although we cannot consider every possible configuration of defect distributions here, these models can describe a trend in the interaction between the dopant and charged vacancies in the context of segregation: model (2) a cation vacancy at the surface; (3) an oxygen vacancy in the bulk; (5) an oxygen vacancy at the surface; (6) a cation vacancy in the bulk; (1) the combination of (2) and (3); and (7) the combination of (5) and (6). There is a dopant in the bulk without any vacancies in model 4, which is assumed to represent the segregation purely due to elastic strain energy and surface polarity.

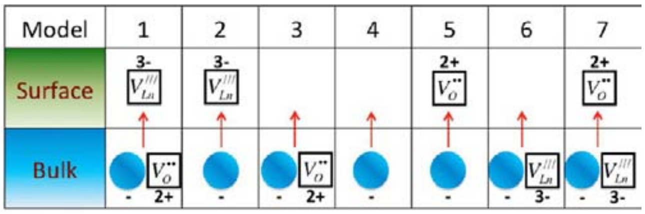

Figure 1. Seven models to represent different electrostatic interactions that are induced by controlling the distribution of charged oxygen and cation vacancies in DFT and analytical models. The blue sphere represents the dopant. Cation vacancy, $V_{Ln}^{///}$, has a formal charge of 3−, and the defect complex of dopant D^{+2} in $V_{Ln}^{///}$ has 1− charge, while $V_o^{\cdot\cdot}$ has 2+ charge state. The numbering from 1 to 7 is in the order of increasing attractive electrostatic force to the dopant at the surface.

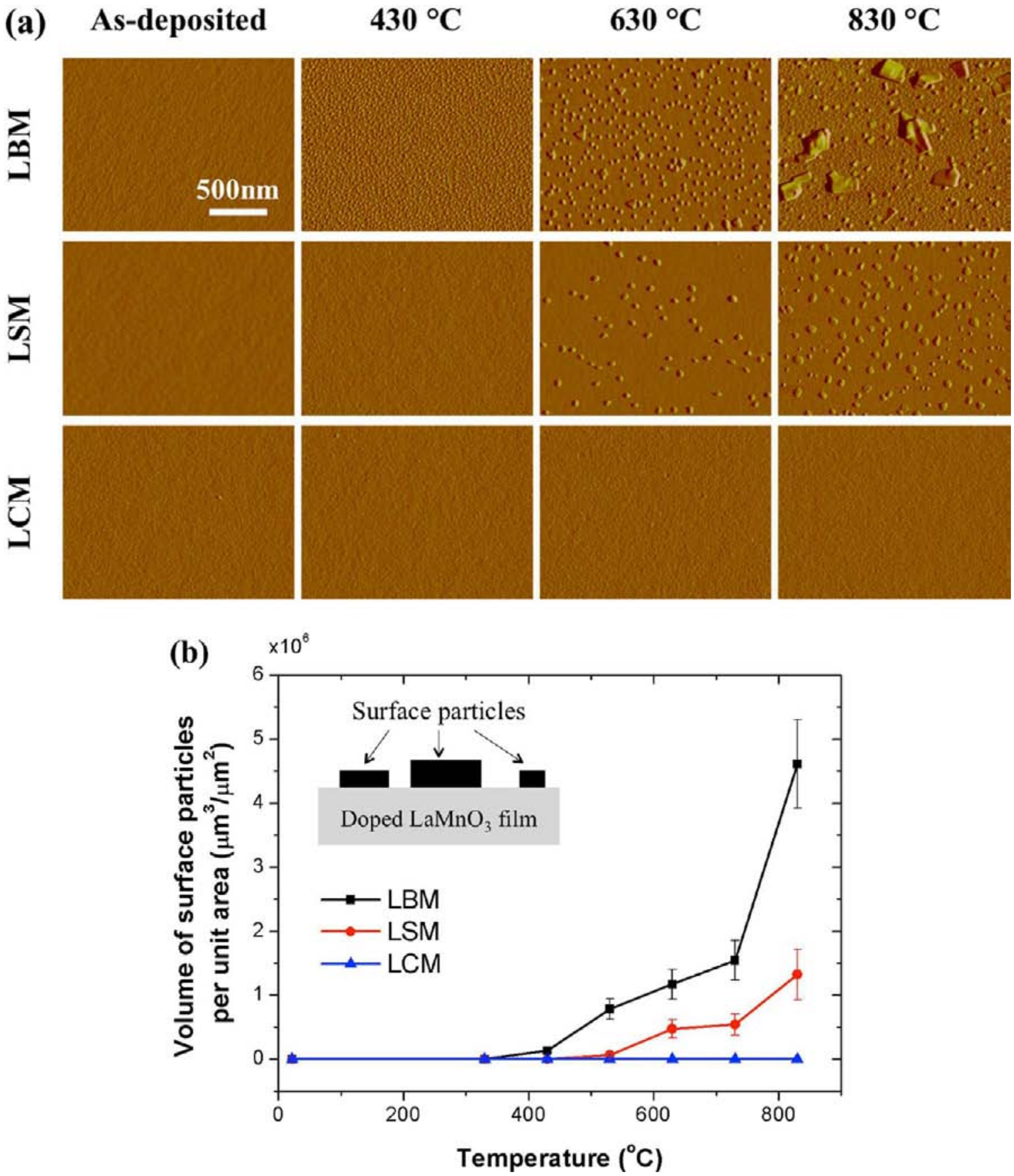

Figure 2. (a) AFM amplitude images of the Ba-, Sr-, and Ca-doped $LaMnO_3$ thin film surfaces as a function of annealing temperature. Each column represents the surface morphology after annealing in air for 1 h at the temperatures stated on the top. Each row represents the surface morphology of LBM, LSM, and LCM. (b) The volume per unit area of the surface particles, calculated from the AFM images, as a function of annealing temperature for LCM, LSM, and LBM.

3. RESULTS AND DISCUSSION

We first present our experimental results which show that: 1) the smaller dopant (Ca) segregates less and maintains a more uniform surface structure compared to the larger cations Sr and Ba (elastic effect), and 2) the low oxygen pressure reduces the extent of dopant segregation due either to the chemical expansion of the lattice (elastic effect) and/or a reduction of the space charge (electrostatic effect) in the doped $LaMnO_3$ films. Next, we computationally assess the dopant segregation quantitatively, explain the governing mechanisms in our experimental findings on $LaMnO_3$ surface, and extend predictively to other materials, in particular the $SmMnO_3$.

3.1. Experimental Results. *3.1.1. Heterogeneous Surface Structure upon Dopant Segregation Correlates with Dopant Size.* First we report the surface structure upon annealing in air (high oxygen pressure) as a function of temperature. Doped $LaMnO_3$ film surfaces showed substantial structural changes upon thermal annealing at elevated temperatures in air, with a clear dependency on the size mismatch between the dopant and host cations. Figure 2a shows the surface morphology of doped $LaMnO_3$ films as a function of annealing temperature (shown at selected temperatures) obtained by tapping mode AFM. As-deposited film surfaces were very uniform and smooth with an RMS roughness of <1 nm. Annealing at high temperatures, however, induced structural changes in the form of surface particles on the film, and the extent of these structural changes followed the order of the size mismatch between the dopant and host cations. Later we will show that these particles are made of dopant-oxides. For LBM films, the surface particles appeared by 430 °C and grew larger and higher upon annealing at higher temperatures. For LSM films, they appeared by 630 °C and grew larger with annealing temperature similarly to LBM films. For LCM films, in contrast, no structural change was found up to 830 °C within the AFM resolution. The temperature at which the particle formation was observed, and the dimension of these surface particles suggests that the LBM films are most active to form such surface phases, followed by LSM and LCM films. Furthermore, the actual amount (volume) of rearranged cations in the form of surface particles also followed the order of the size mismatch. Figure 2b shows the volume of the surface particles per projected unit area (calculated from the AFM images taking into account both the areal size and height profiles) as a function of annealing temperature. The volume of surface particles was the largest on LBM films, followed by LSM, and none for LCM. We note that the size mismatch between the dopant and host cations on the A-site follows the same order, the largest for Ba and the smallest for Ca. This correlation suggests that the elastic energy difference in the system due to the dopant-host cation size mismatch plays an important role in cation rearrangements at the surface; the larger size mismatch drives cation segregation more actively toward the surface to minimize the elastic energy in the system and ultimately form the surface phases. All the chemical analysis presented in the following sections support this argument.

3.1.2. Heterogeneous Surface Chemistry upon Dopant Segregation Correlates with Dopant Size. The changes in surface chemistry, concurrently with the structural changes presented above, were also found to be significant and correlated strongly with the size mismatch between the dopant and host cations. Figure 3 shows the normalized cation intensity ratios from the near-surface region of the doped $LaMnO_3$ thin films with the three dopants. The detailed quantification and normalization process was described in Section 2.1.2. Dopant-to-Mn (D/Mn) ratios increased with the annealing temperature (Figure 3a). The chemical changes upon annealing were larger with the larger size mismatch between the dopant and host cations, consistently with the structural changes observed by AFM. LBM films (the largest size mismatch) showed the greatest increase in D/Mn ratios, followed by LSM films. LCM (the smallest size mismatch) films showed the smallest extent of dopant segregation at the surface. The observed dependency of structural and chemical changes on the size mismatch among the A-site cations substantiates that the elastic energy minimization plays a key role in cation rearrangements as a driving force. However, clearly the size mismatch is not the only player, because even Ca was found to enrich at the surface despite the fact that its size deviates from La only a very small fraction. Moreover, Figure 3b shows that the dopant-to-La (D/La) ratios also increased with annealing temperatures similarly to the behavior of D/Mn ratios in Figure 3a. The increase of D/Mn and D/La ratios concurrently with the appearance of surface particles indicates that these surface particles are mainly composed of the dopant cations. The high-resolution analysis of the core level photoemission spectra of the dopant cations with different emission angles was performed to enable a quantitative analysis of the chemical environment as a function of depth from the film surface in a nondestructive way.[1,30] This analysis helps to deduce if the dopant segregation is associated with a secondary phase formation or if it takes place on the perovskite-terminated lattice. The concomitant increase of surface components with the total increase of dopant content at the surface indicates that the segregated dopant may form a nonperovskite coordination at the surface (see Figures S3 and S4).

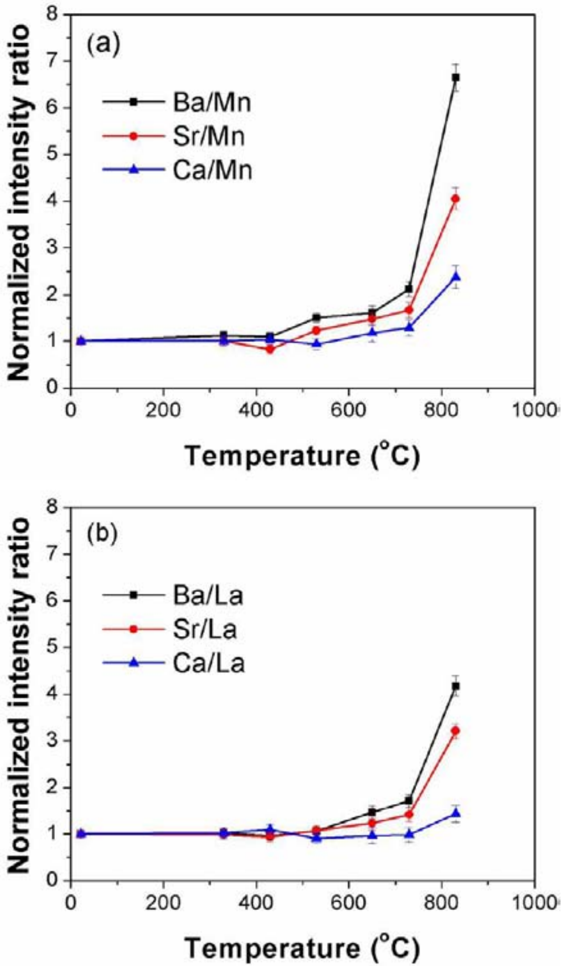

Figure 3. Normalized cation intensity ratios quantified by AR-XPS and AFM as a function of annealing temperature. (a) D/Mn and (b) D/La ratios.

Formation of dopant-enriched secondary phases, which was inferred from the analysis in Figures S3 and S4, was further supported by subsequent localized measurements of chemical composition using AES. Figure 4a−d shows the elemental maps on LBM films annealed at 830 °C. Brighter color represents higher intensity of each element. A higher concentration of Ba and lower concentrations of La and Mn were found in the surface particles. Figure 4e,f shows the localized chemical intensity ratios acquired on top of surface particles (solid markers) and away from those phases (open markers). A significantly higher concentration of Ba in surface particles was found compared to that on the as-deposited films, substantiating that these particles are mainly composed of Ba in secondary phases. Away from those phases, however, the concentration of Ba was lower than that on the as-deposited films, indicating the depletion of Ba on those regions. From this we conclude that the dopant cations separate out from the near-surface region,

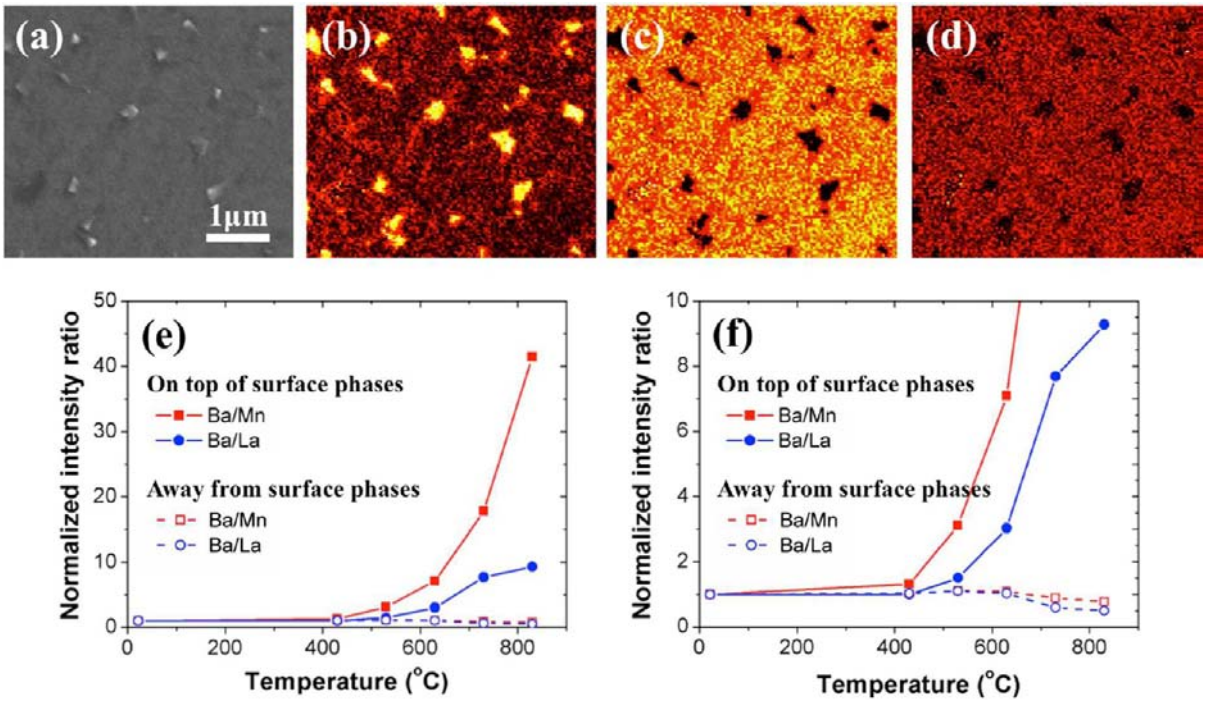

Figure 4. (a) SEM image on the annealed LBM films, and AES elemental maps deduced from (b) Ba MNN, (c) La MNN, and (d) Mn LMM. Point spectra on top of surface particles (solid markers) and away from surface particles (open markers): (e) normalized cation intensity ratio in full scale, and (f) plot that is zoomed into the maximum intensity ratio of 10 from (e).

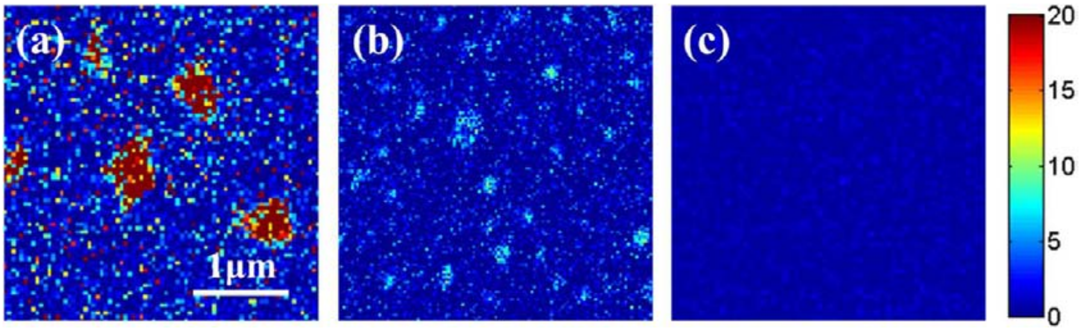

Figure 5. Cation intensity ratio maps on the three films after annealing at 800 °C for 1 h. (a) Ba/Mn on LBM, (b) Sr/Mn on LSM, and (c) Ca/Mn on LCM.

cluster, and form the surface phases with a heterogeneous distribution, causing the depletion of dopant cations away from the surface particles. This behavior is similar to the Sr segregation structure that we found on LSC films in our prior work.[1] The LSM film surfaces in this work also behaved similar to the LBM films—agglomeration of Sr to form the surface particles and depletion of Sr on the rest of film surface (see Figure S5). The LCM films, however, showed no noticeable formation of surface particles after annealing up to 830 °C, as shown in Figure 2.

We now turn our attention to the dependence of the geometry and chemistry of the surface heterogeneities on the dopant size. Figure 5 compares the D/Mn intensity ratios deduced from AES maps on the three films after annealing at 830 °C in air for 1 h. LBM and LSM films showed formation of surface particles that were secondary phases with dopant enrichment in them, while LCM films showed a uniform distribution of cations. Lateral dimension of these surface phases reveals that they were the largest on LBM films and that no noticeable formation of such heterogeneous secondary phases existed on LCM films. This behavior is consistent with the AFM analyses of surface particles in Figure 2. D/Mn ratios show that the dopant enrichment at the surface is the highest on LBM films and the least on LCM films, consistently with the AR-XPS analyses shown in Figure 3.

From the structural and chemical analysis presented thus far, we conclude that: (1) the size mismatch between the dopant-host cations contribute significantly to the segregation of the dopant cations and secondary phase formation at the surface; (2) the larger size mismatch results in more cation rearrangements; and (3) dopant cations separate out more actively than the host cation to form dopant-rich secondary phases that are distributed heterogeneously at the surface. This dependency on the size mismatch substantiates that the elastic energy minimization plays an important role in cation rearrangements as a driving force. The larger ionic radius of the Ba^{2+} and Sr^{2+} than the La^{2+} ions is associated with larger lattice distortions compared to that with Ca^{2+}. The elastic energy in the doped $LaMnO_3$ films is minimized, and a thermodynamic equilibrium is reached by pushing the misfit dopants to the surface and

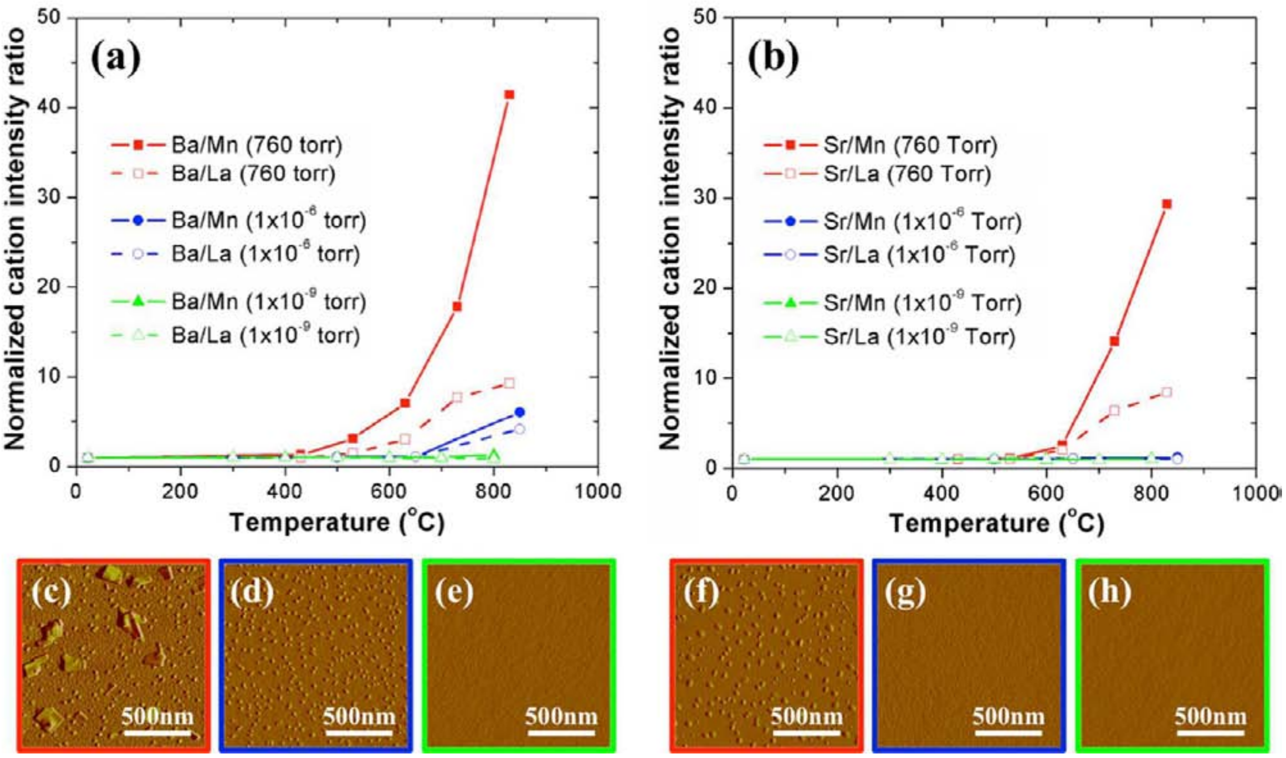

Figure 6. Normalized cation intensity ratios from point analyses using AES on (a) LBM and (b) LSM films. Surface morphology of LBM films after annealing at (c) 830 °C in 760 Torr, (d) 850 °C in 1×10^{-6} Torr, and (e) 800 °C in 1×10^{-9} Torr. Surface morphology of LSM films after annealing at (f) 830 °C in 760 Torr, (g) 850 °C in 1×10^{-6} Torr, and (h) 800 °C in 1×10^{-9} Torr.

relieving the accumulated strain in the film during annealing.[78] The relatively higher chemical stability of the Ca-doped $LaMnO_3$ film surface can then be ascribed to the relatively small size of Ca^{2+} that is very close to the size of La^{2+}. Thus, it is easier to accommodate Ca^{2+} in the bulk $LaMnO_3$ compared to the Ba^{2+} and Sr^{2+} cations. Indeed, the Ca-doped $LaMnO_3$ films showed a relatively smaller amount of dopant segregation, but there still existed Ca enrichment at the surface at elevated temperature despite its matching size to La^{2+}. This is where the electrostatic interaction must also be taken into account.

3.1.3. Oxygen Pressure Affects the Dopant Segregation via Lattice Parameter and Charged Defect Distribution. We hypothesized that the elastic and electrostatic energy minimization together are responsible for describing the aforementioned cation rearrangements at the surface at elevated temperature. Here we provide another parameter, the oxygen pressure, as a means to deduce partially the effect of the elastic and electrostatic interactions of the dopants with the surface. The quantitative assessment of the contribution of the elastic and electrostatic energy to the cation rearrangements will be discussed with the theoretical and computational results in the Section 3.2 in detail.

By varying oxygen partial pressure, we impact the material structurally by expanding or contracting the oxide films, by the so-called 'chemical expansivity' phenomenon[78−82] (associated with the elastic energy) and chemically by altering the distribution of charged point defects and localized electrons (associated with the electrostatic interaction). First, the oxygen pressure during annealing changes the lattice parameters of perovskite oxide films: the higher oxygen pressure incorporates oxygen into the lattice and contracts the lattice, while the lower oxygen pressure expands the lattice upon oxygen loss.[78,83−85] The changes in the lattice parameter directly couple to the elastic energy of the thin films as the driving force for cation rearrangements. Second, because the formation energy of oxygen vacancies is typically smaller at the surface compared to the bulk of oxides,[63,64] a high concentration of oxygen vacancies is expected on the top surface compared to bulk. Beneath the positively charged surface of a mixed ionic electronic conductor oxide, a space charge layer can exist with an increase in electron concentration. By decreasing the oxygen pressure and reducing the doped Manganite films, the electronic charge carrier density increases, and thus the Debye screening length would decrease. Therefore, one can expect a decrease in the spatial extent and strength of the space charge region in reducing conditions. Such changes in the redistribution of positively charged oxygen vacancies and negatively charged electrons couple to the electrostatic energy.

To assess the effects of oxygen pressure during annealing on the surface chemistry and structure, three oxygen pressures were considered, 760 Torr (air), 1×10^{-6} Torr, and 1×10^{-9} Torr. Normalized cation intensity ratios were acquired by a point analysis of AES on top of surface phases (or from the background film surface if no secondary features existed). The extent of dopant segregation was found to be largest for thin films annealed in air (760 Torr) and to decrease with decreasing oxygen pressure, as shown by the D/Mn and D/La ratios in Figure 6a,b for the LBM and LSM films, respectively. The changes in surface morphology (Figure 6c−h) were the largest after annealing in the highest oxygen pressure, while no noticeable changes were observed in the lowest oxygen pressure. Combined structural and chemical investigation clearly demonstrates the effects of the oxygen pressure during annealing: the higher oxygen pressure drives

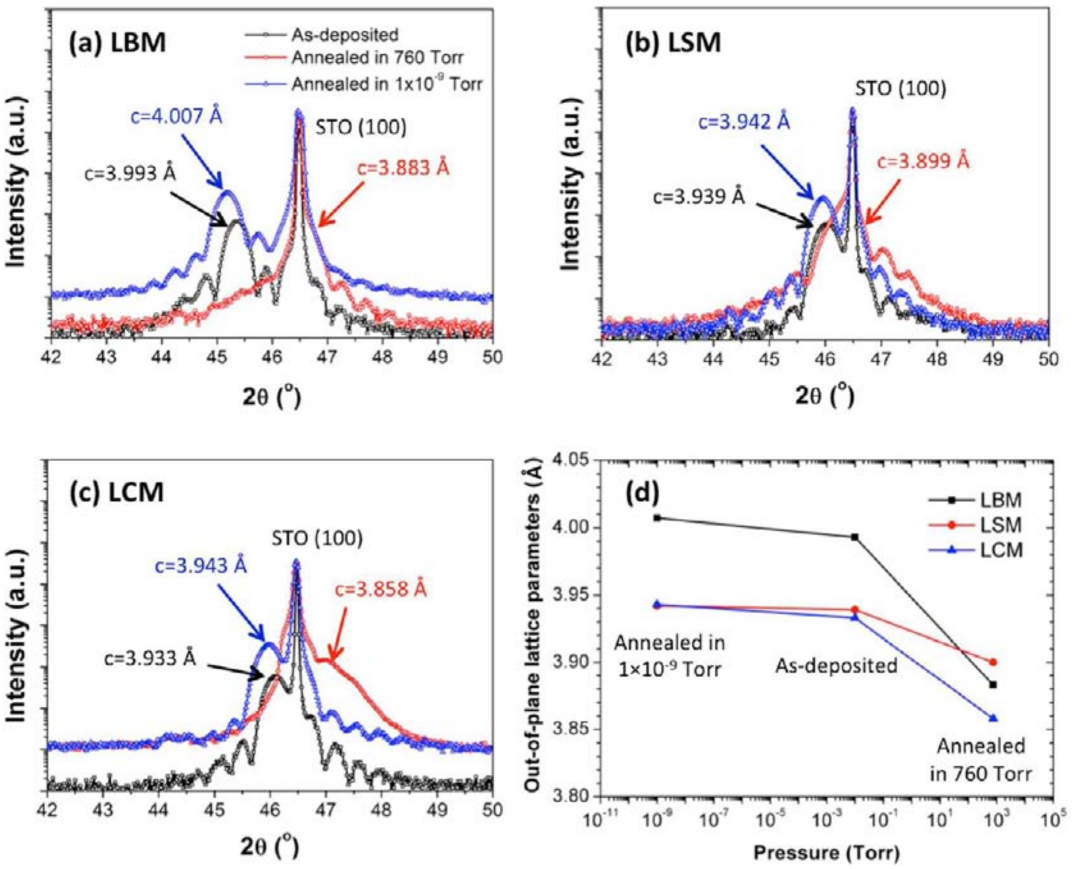

Figure 7. High-resolution XRD patterns with out-of-plane lattice parameters at each process step of (a) LBM, (b) LSM, and (c) LCM films. Black, red, and blue lines represent the as-deposited, annealed in 760 Torr, and annealed in 1 × 10^{-9} Torr, respectively. (d) Out-of-plane lattice parameters of three films at each process step as a function of pressure.

cations more toward the surface with segregation and secondary phase formation. Note that the dependency of cation rearrangements on the size mismatch among the host-dopant cations was still prevalent in the different oxygen pressures. After annealing in 1 × 10^{-6} Torr oxygen, e.g., LBM films showed sizable changes in the chemistry and structure at the surface, while LSM films did not show any discernible changes at or below 1 × 10^{-6} Torr.

This dependency of surface segregation on oxygen pressure found on the LBM, LSM and LCM films in this work was similar to that found on $La_{0.6}Sr_{0.4}Co_{0.2}Fe_{0.8}O_3$,[86] whose underlying reasons were not presented before. We make another analogy here to a recent result reported on the effect of electrochemical potential on the Sr segregation on $La_{0.75}Sr_{0.25}Cr_{0.5}Mn_{0.5}O_{3\pm\delta}$ thin film model electrodes.[87] In that work, cathodic polarization (reducing condition) was found to decrease the strontium surface concentration, while anodic polarization (oxidizing condition) increased the strontium accumulation at the electrode surface. However, the underlying mechanisms were not clarified.

As noted above, there are two possible mechanisms that we hypothesized, by which the lower oxygen pressures can impact the surface dopant segregation: via the chemical expansion of the lattice and via the change in the concentration and distribution of oxygen vacancies. In support of the first, substantial changes of the out-of-plane lattice parameters were found as a function of oxygen pressure. Figure 7 shows the high-resolution XRD patterns for the LBM, LSM, and LCM films with out-of-plane lattice parameters at each process step (as-deposited, annealed in 760 Torr, and annealed in 1 × 10^{-9} Torr). The lattice parameters decreased after annealing in the high oxygen pressure due to oxygen incorporation into the lattice and increased after annealing at low oxygen pressure due to oxygen loss from the lattice. The out-of-plane lattice parameter of the as-deposited films (e.g., 3.993 Å for LBM) being higher than that of the bulk (e.g., 3.891 Å for LBM) showed that the films were oxygen deficient. It is known that manganite films prepared by PLD are usually oxygen deficient with larger out-of-plane lattice parameters.[85,88,89] After annealing at 830 °C in 760 Torr, the out-of-plane lattice parameter decreased (e.g., to 3.883 Å from 3.993 Å for LBM). Annealing in the high oxygen pressure oxidizes Mn^{3+} to Mn^{4+} upon oxygen incorporation, resulting in the decrease of the out-of-plane lattice parameter.[89−91] After annealing at 800 °C in 1 × 10^{-9} Torr, in contrast, the out-of-plane lattice parameter increased (e.g., to 4.007 Å from 3.993 Å for LBM). At the low oxygen pressure, the oxygen vacancy formation in the films reduces Mn^{4+} to Mn^{3+}, resulting in an expansion of lattice unit cell.[78,85,88−91] The in-plane lattice parameters were expected to remain constant upon annealing because of the epitaxial coherency to the substrate.[85] The changes in the out-of-plane lattice parameters directly affected the volume in the films and, hence, the elastic strain energy in the system. This directly levers the tendency to cation rearrangements at the surface. Decrease in the out-of-plane lattice parameters upon annealing in 760 Torr (or upon oxygen uptake) drives the cations to segregate toward the surface to minimize the elastic energy in the system. Annealing in 1 × 10^{-9} Torr, however, increased the

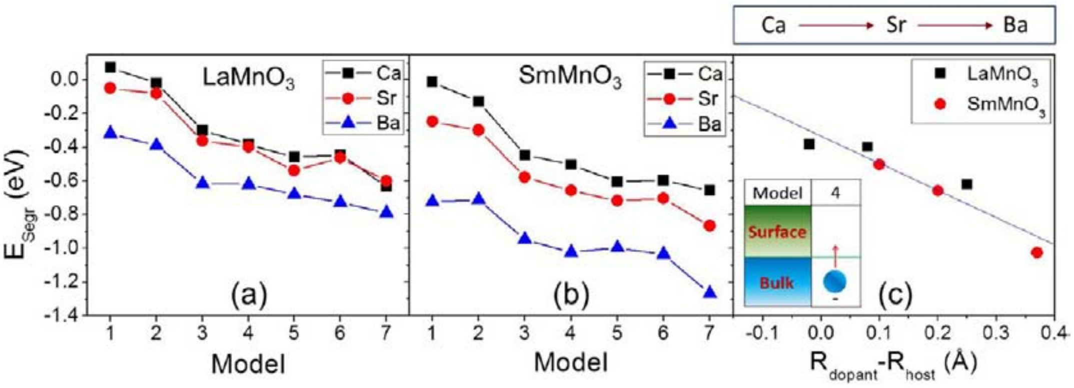

Figure 8. Surface segregation energies of Ca, Sr, and Ba dopants on (a) LaMnO$_3$ and (b) SmMnO$_3$ surfaces within the different electrostatic interaction models (1−7) described in Figure 1. Recall that the electrostatic attraction of the dopant to the surface increases from models 1 to 7. (c) E_{segr} for model 4 on LaMnO$_3$ and SmMnO$_3$ as a function of $R_{dopant} - R_{host}$. The model 4 is illustrated in the inset.

out-of-plane lattice parameters. Such chemically expanded lattice provides more space to accommodate the larger dopant cations in the bulk lattice, reducing the dopant elastic energy and suppressing the dopant segregation at the surface.

In relation to the second mechanism by which oxygen pressure can affect dopant segregation, we provide the following discussion. Annealing at high temperatures reduces the oxide film and creates oxygen vacancies. The concentration and distribution of created oxygen vacancies depend on the oxygen pressure during the annealing. Approximately 10^6 times higher vacancy concentration at the surface than in the bulk (10^{-3} on surface and 10^{-9} in bulk) was predicted for La$_{0.9}$Sr$_{0.1}$MnO$_3$ under typical SOFC operating conditions at pO_2 = 1 atm and 1173 K.[63] Such higher concentration of oxygen vacancies at the top surface form a positive core compared to the bulk of the film. The space charge effects with a positive surface and a negative subsurface[27,66,67] (discussed in Section 2.2.2.2) results in a strong Coulombic attraction of the dopant cations to segregate toward the surface (see Figure S6 and bottom right in Figure 12). Note that the width of this space charge layer is expected to be narrow because of the short (~1 nm) screening length for heavily doped LaMnO$_3$.[68] Annealing in the very low oxygen pressures (10^{-6} to 10^{-9} Torr), on the other hand, creates a large concentration of oxygen vacancies throughout entire thickness of the oxide films because of the reduction in the free energy of vacancy formation at the low oxygen chemical potential. Furthermore, the concentration gradient of oxygen vacancies when annealed in the low oxygen pressures increases, e.g., going from 10^{-5} in the bulk to 10^{-1} at the surface of La$_{0.9}$Sr$_{0.1}$MnO$_3$ at $pO_2 = 10^{-9}$ atm and 1173 K.[63] Therefore, we expected a greater segregation of the dopant as the oxygen pressure decreases. However, we observed the opposite: dopant segregation decreased significantly with lowering the oxygen pressure in our experiments. This can be attributed to two possible hypothesis: first one related to the weakening of the electrostatic driver, and the second one related to the dominating extent of chemical expansion discussed above. The first can arise due to a change in the distribution of localized electrons. By decreasing the oxygen pressure and reducing the doped manganite films, the charge carrier density increases, and thus the Debye screening length would decrease. Therefore, one can expect a decrease in the spatial extent and strength of the space charge region beneath the surface in reducing conditions and a weakening of the electrostatic attraction of the negatively charged dopant defects to the surface. The second hypothesis is based on the lattice expansion in reducing conditions. The observed lattice expansion of these manganite films in the low oxygen pressure (recall Figure 7) is substantial. Such a large chemical expansion (keeping the dopant cations in the bulk lattice) can dominate even if there were an increase of electrostatic attraction to the dopant cations and suppress the cation segregation tendency at the surface in low oxygen pressure. In this experiment, we have direct experimental proof for the chemical expansion effect, and we believe that one to be the dominant mechanism reducing the segregation at the lower oxygen pressures that we surveyed.

We excluded the possibility that the lower formation enthalpies of oxides and/or carbonates cause the different tendency to cation rearrangements. The standard formation enthalpies of bulk oxides and carbonates, however, provide no evidence to describe the observed trends in cation rearrangements (Table S2). Furthermore, the surface carbonate phases, including BaCO$_3$, SrCO$_3$, CaCO$_3$, La$_2$(CO$_3$)$_3$, and MnCO$_3$, could be excluded on our samples due to the absence of a C 1s peak corresponding to the carbonate signature at temperatures above 500 °C (Figure S7). Lastly, when independent samples were annealed in pure O$_2$, the formation of secondary phase particles and the substantial increase in the D/Mn and D/La ratios at the surface were found again (Figures S8 and S9), very similar to the films annealed in air reported here. This similarity substantiates that the secondary phase formation involves mainly O$_2$ and not CO$_2$. As a result, we deduce that the secondary phases at the surface were dopant-enriched oxides and/or hydroxides rather than dopant-enriched carbonates.

3.2. Computational Results.

As discussed above, it is difficult to quantitatively separate out the structural and chemical effects of the oxygen pressure on the dopant segregation at the surface in experiments, while both effects can play a significant role. However, we turn now to computational results to show explicitly that charged defect interactions also play an important role in the segregation of dopants and explain quantitatively the concerted role of both the elastic and electrostatic energy on this phenomenon. We note that the space charge effects described above are beyond the size scales that can be captured by DFT models currently. Therefore, we assessed the effect of charged defect distribution from the surface to the bulk of the LnMnO$_3$ films using hypothetical models without having to constrain the near-surface configuration as a space charge. In this way, we also generalize the role of electrostatic interactions in cation

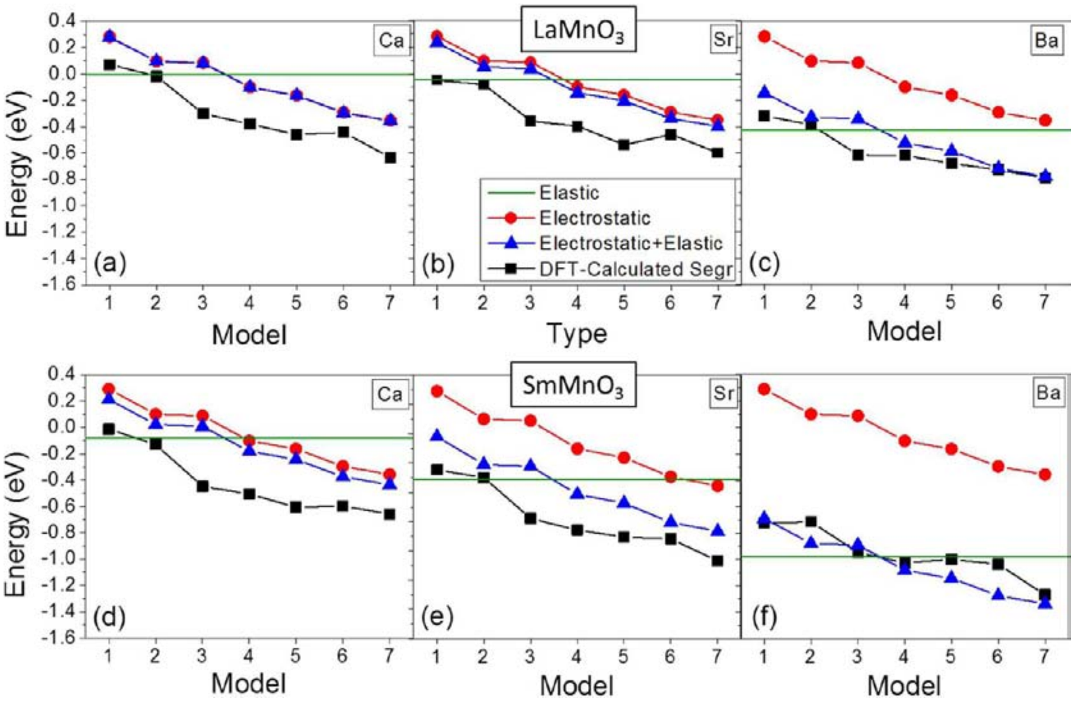

Figure 9. Comparison of the DFT-calculated total segregation energy, E_{segr}, with the one calculated analytically as the sum of the elastic and electrostatic energy. The green, red, blue and black lines denote the analytically calculated elastic energy, electrostatic energy, sum of electrostatic and elastic energies, and DFT-calculated E_{segr}, respectively, as a function of models 1–7.

segregation regardless of the strength of space charge in a given composition.

3.2.1. Dopant Segregation Driven by Elastic and Electrostatic Energy. Dopant segregation energy, E_{segr}, for the seven electrostatic interaction models with the three dopants on both $LaMnO_3$ and $SmMnO_3$ surfaces obtained from our DFT+*U* calculations and eq S1 are shown in Figure 8a,b. For both materials, two distinct trends are found: (1) the larger dopant cation segregates more strongly toward the surface; and (2) the model where the dopant experiences the larger electrostatic attraction to the surface and the larger electrostatic repulsion from the bulk shows a stronger tendency to enrich the dopant at the surface. For model 4, where there are no charged defects in the system, the negative segregation energy arises from the elastic energy effect as well as the electrostatic interaction of the dopant with the polar surface[49] on the $LnMnO_3$ films. According to eq 1, elastic energy depends on the size difference between the host and dopant cations. If we plot E_{segr} from the DFT calculations for model 4 on each surface as a function of $R_{dopant} - R_{host}$, we observed an almost linear correlation between them (see Figure 8c). For both the $LaMnO_3$ and $SmMnO_3$ surfaces, therefore, the largest dopant, Ba (blue marks and line in Figure 8a,b), introduces the largest elastic energy into the system and, thus, is associated with a larger (negative) segregation energy and strongest tendency to enrich at the surface. The radius of Sm cation is smaller than that of La, and this causes a larger size difference of the host with respect to the dopants. Therefore, the segregation tendency of all three dopants on the $SmMnO_3$ surface was greater than that on the $LaMnO_3$. Importantly, we note that the predicted dependency of the segregation energy on the dopant size was well consistent with the surface chemical and structural analyses on the doped $LaMnO_3$ films in our experiments, reported in Figures 2–6. This consistency with the experimental results as well as the predictive extension of this behavior to $SmMnO_3$ by our calculations confirm that indeed the elastic energy minimization is an important contributor to dopant segregation on perovskite oxides.

It is clear that the electrostatic interaction variation in our models only depends on the distribution of oxygen and cation vacancies. Therefore, it is independent of the size of the dopant and host cations. We confirm this by plotting the changes in E_{segr} in Figure 8a,b relative to the E_{segr} of model 4 where there are no charged vacancies. In this case, all the relative segregation energies for each dopant converge approximately into one line that is consistent with the electrostatic energy obtained by Coulomb's law for each defect configuration (see Figure S10). This result clearly demonstrates that the electrostatic interaction of the dopant with the lattice defects is also an important contributor to dopant segregation on perovskite oxides.

3.2.2. Deconvoluting the Contributions of the Elastic and Electrostatic Energy in Dopant Segregation. Our next goal is to resolve quantitatively the contribution from the elastic and electrostatic interactions to the dopant segregation at the surface and to examine if indeed E_{segr} can be represented as the sum of $E_{elastic}$ and $E_{electrostatic}$. As we noted in the previous section, it has been impossible to entirely decouple these two contributions experimentally, even when we varied the oxygen pressure. For this purpose, we used the analytical models (Section 2.2.2) to calculate both the elastic and electrostatic energies and compared them to the DFT-calculated total segregation energies. For each dopant, the elastic energy is constant over the seven electrostatic models but strongly depends on the size difference between the dopant and the host cations. On the other hand, the electrostatic energy is shown with the same red curve in Figure 9a–f as function of the type of the defect configuration model but independent of the

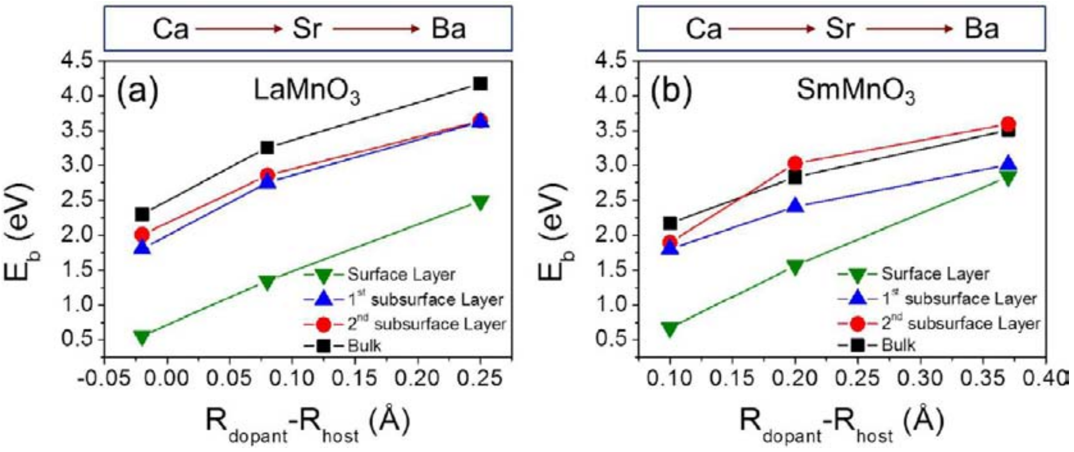

Figure 10. Migration energy barrier, E_b, of cation vacancies in (a) $LaMnO_3$ and (b) $SmMnO_3$ as a function dopant cation (size mismatch between the dopant and host cations, $R_{dopant} - R_{host}$) for diffusion of the dopant between each atomic layer from the surface into the bulk.

dopant-host cation size mismatch. The two energy contributions are added (blue lines in Figure 9a–f) to compare them with the DFT-calculated total E_{segr} (black line in Figure 9a–f). Overall, the sum of two energy contributions was in reasonable agreement with the DFT-calculated E_{segr} on both surfaces within 0.16 ± 0.15 eV, which demonstrates that the elastic and electrostatic energies are two important contributors to the segregation phenomenon. Especially for the Ba dopant, the agreement was seemingly very good within 0.01 ± 0.14 eV. For Ca and Sr dopants, however, the sum of the two energy contributions from the analytical models underestimated the DFT-calculated E_{segr} by 0.24 ± 0.09 eV. Such deviation between the DFT calculated E_{segr} and that calculated from the elastic and electrostatic energy models among all compositions is attributed to the possibility of other contributors, such as the surface polarization effect on manganites[92−94] that we did not explicitly assess. However, we emphasize that the surface polarization effect is inherently present in our DFT calculations. This can be realized from the negative E_{segr} value even for model 4 in Ca-doped $LaMnO_3$, where no charged vacancies are present and where the size of Ca and La is very close to each other.

Inaccuracies in the analytical models are also among the possible sources of the deviation between the DFT results and the analytical model results. Friedel equation[61] (eq 1) cannot perfectly describe our system due to its limitations as noted above; the dopant concentration in our model is not infinitely dilute, and due to the limited size of our supercell, the lattice strain energy induced by the larger dopant would not be fully relaxed upon the segregation. In addition, for elastic energy calculations, we have used Shannon's ionic radii that are valid for purely ionic systems; on the other hand, the perovskite systems that we deal with here are not fully ionic. For electrostatic energy, Coulomb's law (eq 2) was employed, but it is also valid for the purely ionic materials. In spite of these, Figure 9 clearly shows that the elastic and electrostatic energies are major contributors to the segregation of dopant on the $LnMnO_3$ surfaces.

Based on the results in Figure 9, it is possible to predict the segregation energy to a large extent simply by the sum of the elastic and electrostatic energies that can be calculated from the analytic models described in Section 2.2.2. Using these models can make an efficient route to estimate the trends in the enhancement or depletion behavior of dopants on a range of perovskite oxides without having to perform many of the computationally expensive DFT calculations. For the different types of perovskite oxides, the elastic and electrostatic contributions to the E_{segr} would vary. For example, LSC, another widely studied SOFC cathode,[28,95−97] is known to be a relatively more elastic material than LSM with a Young's modulus (64.4 GPa for $La_{0.8}Sr_{0.2}CoO_3$ at room temperature)[98] smaller than that of LSM (129 GPa for $La_{0.67}Sr_{0.33}MnO_3$ at room temperature).[99] LSC also reduces more easily to form more oxygen vacancies at the surface compared to LSM,[100] inducing larger electrostatic attraction to the dopants. We can therefore expect that the elastic energy contribution to dopant segregation on LSC is less, while the electrostatic energy contribution is more compared to that on LSM.

3.2.2. Diffusion Kinetics of Dopant Cations. Sections above discussed the driving forces to segregation in the context of thermodynamics of this phenomenon. Kinetics of the unit processes involved in the segregation is also important to consider because at a given temperature and time, the surface composition is an outcome of the combined effects of thermodynamics and kinetics. For this purpose, the diffusion of segregating cations must be carefully considered. We performed Nudged Elastic Band (NEB) calculations for cation diffusion with the vacancy exchange mechanism for each dopant and host cation in the bulk and near the surface of the $LnMnO_3$ system. The faster a cation diffuses, the quicker it can enrich at the surface given a driving force to it to migrate to the surface. Opposite to the results from the thermodynamic driving role of the elastic energy (Section 3.2.1), the larger cation was found to diffuse slower toward the surface with a higher migration energy barrier (Figure 10). For example, Ba dopant has ~1.9 eV higher migration barrier than Ca both in the bulk and at the surface of $LaMnO_3$. This suggests that, while Ba is more strongly driven to the surface due to elastic energy minimization, its high migration barrier would lead to slower segregation kinetics. At reduced temperatures, the segregation process of the large cation may be kinetically hindered.

Overall the migration barriers for these cations in the bulk of the manganites were predicted to be large, ranging as ~2.2−4.2 eV. The considerably large migration barrier of cation vacancies in the bulk perovskite oxides was also reported in the literature; calculated values of 3.93 eV in $LaMnO_3$,[101] 4.70 eV[102] or 4.52 eV[103] in $LaGaO_3$, and 4.00 eV in $LaFeO_3$[104] for La vacancy

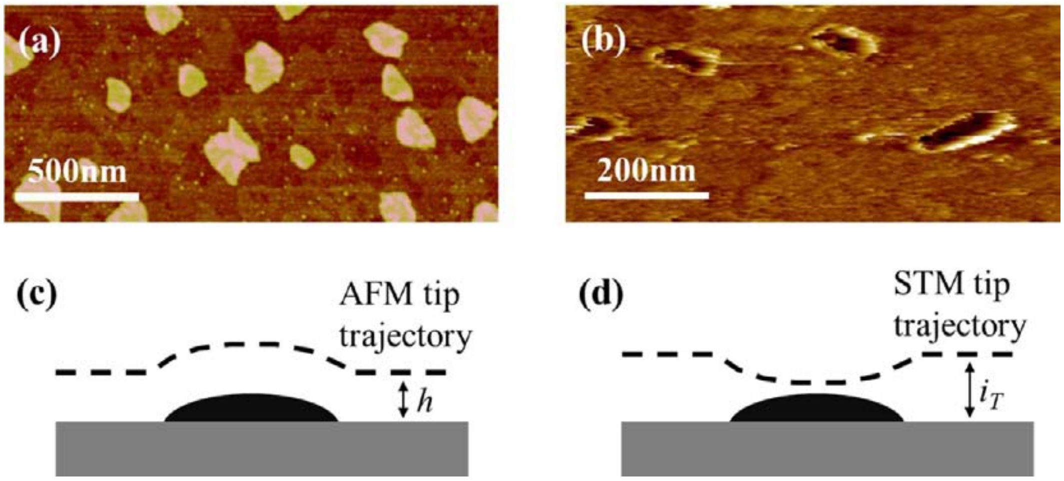

Figure 11. Surface morphology of LSM films after annealing at 830 °C in air (a) by AFM and (b) by STM. The imaging mechanism is illustrated schematically (c) for AFM and (d) for STM. The dashed line represents the tip trajectory; *h* represents the true separation distance between the tip and the sample in AFM imaging; and i_T represents constant tunneling current that is maintained by varying the separation distance if the surface is electronically heterogeneous.

diffusion, and experimental activation energy of 4.98 eV in $LaCrO_3$[105] and 3.32 eV in $LaFeO_3$[106] for La diffusion. This range of values is consistent with our DFT results in Figure 10. More importantly, we found that the migration barrier of these cations was significantly lower at the near surface (i.e., from the first subsurface layer to the surface) than in the bulk, by ~1.5 eV on both the $LaMnO_3$ and $SmMnO_3$ considered here. Specifically, we examined the change in the diffusion barrier of cation vacancies as a function of distance from the surface. For both materials, the cation migration was more facile as the position was closer to the top surface. This is attributed to the easier relaxation and flexibility of the structure near the surface, causing the dopant to migrate more easily than in the bulk.[107,108] As a result, the spatial extent of cation segregation is expected to be limited to the near-surface region and is not spread largely to the bulk of the material unless at very high temperatures.

3.3. Implications to Electronic Properties and Electrochemical Activity. The heterogeneous chemistry observed at the surface of the LBM and LSM films upon dopant segregation is expected to be associated with a heterogeneously distributed electronic and electrochemical behavior at the surface. Here we attempt to infer the impact of cation segregation and phase separation on the ORR kinetics at the cathode surface. Specifically, we investigated the correlation between the chemical heterogeneity and the electron-transfer properties at the surface by contrasting the images obtained from two scanning probe techniques, AFM and STM. The result is demonstrated for LSM in Figure 11 that shows the surface image of LSM films after annealing at 830 °C in air with the two techniques. Interestingly, surface particles, which we confirmed to be secondary phases, appeared with similar lateral dimensions and shapes but with opposite height contrast—protrusions with AFM scanning (i.e., higher profiles compared to the film surface) and depressions with STM scanning (i.e., lower profiles compared to the film surface). This contrast originates from the different sources for height profile information in these two techniques.[109] AFM scanning is associated directly with the true geometrical height. In contrast, the STM scanning is associated with the density of states at given bias voltage between the tip and the sample. Even if the feature is geometrically protruding from the surface, it appears depressed if the feature is less conducting or insulating compared to the rest of the film surface. This observation is supported by the drastically different energy gaps between the pristine LSM film and insulating SrO phases; 2.1−2.6 eV for LSM films from our previous work[30,33] and 5.7−5.9 eV for SrO.[110] Therefore, this image contrast provides a direct evidence that the secondary phases formed upon dopant segregation are electronically more insulating than the rest of the film surface. Such insulating phases hinder the charge transfer on the cathode surfaces, lowering the rate of oxygen reduction on the cathode.[1,34,111,112] Annealed LBM film surfaces also showed a similar contrast between the AFM and STM images, presented in Figure S11.

4. CONCLUSION

We demonstrated that the dopant cations on the A-site segregate toward the surface of the manganite-based perovskite oxides to minimize the elastic energy due to a mismatch of the dopant and host cation sizes and to minimize the electrostatic energy due to the interactions between the dopant and the charged defects at the surface and in the space charge zone near the surface, in addition to the surface polarity effects discussed earlier.[49] To systematically induce elastic energy differences in the model system, $LnMnO_3$, we varied the radius of the selected dopants (Ca, Sr, Ba) with respect to the host cations (La, Sm) while maintaining the same charge. In annealing experiments, we varied the oxygen chemical potential, whose expected impact is 2-fold: elastic energy via the chemical expansion and the electrostatic interactions via the redistribution of charged defects near the surface. The integration of XPS, AES, XRD, AFM, and STM in our approach enabled us to characterize the extent of dopant segregation and structural transformations at the surface of model dense thin films. DFT calculations and analytical models enabled us to interpret our experiments, to quantitatively decouple the contributions of the elastic and electrostatic energy to the segregation thermodynamics, and to assess the kinetics of dopant diffusion. We found that the assessment of segregation energies based on the dopant elastic energy and electrostatic energy is reasonably accurate compared to the DFT results. This provides a practical means

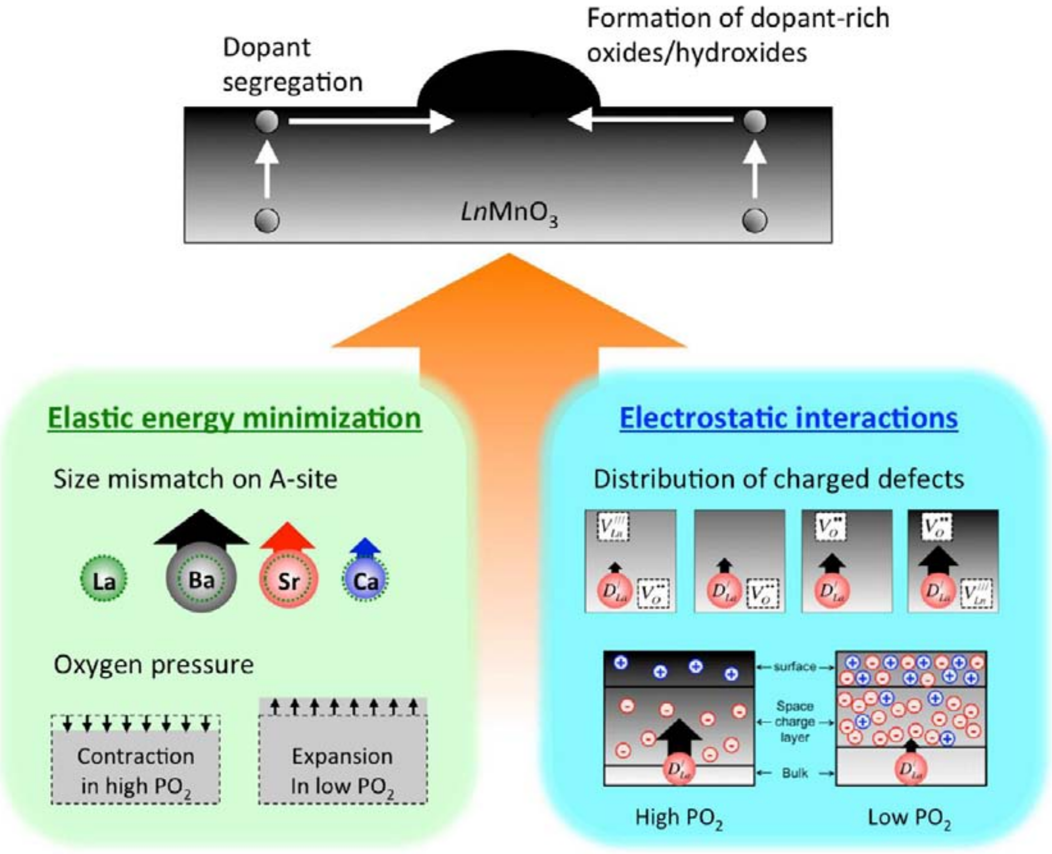

Figure 12. Illustration of the mechanisms that drive dopant segregation to the surface of $LnMnO_3$.

to predict and design perovskite oxide composition with minimal detrimental effects of cation segregation. Our findings on the dopant segregation behavior are summarized in Figure 12.

A smaller size mismatch between the host and dopant cations was found to suppress dopant segregation. In this study, the least segregation at the surface was predicted computationally for the Ca−La pair (the most for the Ba−Sm pair), and the same was observed experimentally. The diffusion kinetics of the larger dopants, Ba and Sr, was found to be slower and can kinetically trap the segregation at reduced temperatures despite the larger elastic energy driving force. Because the cation migration was found to be more facile closer to the top surface, the spatial extent of cation segregation is expected to be enhanced in the near-surface region. The dopant segregation is significant at the high oxygen pressure and was found to decrease in the low oxygen pressure at the same elevated temperatures. This was attributed to two possible mechanisms. First is the chemical expansion of the doped $LaMnO_3$ in the low oxygen pressures and contraction in the high oxygen pressures. In the former, the bulk lattice expands to accommodate the misfit large dopants and reduces the dopant strain energy. Second is the change in the distribution of charged species near the surface. In low oxygen pressure, the space charge effect is expected to decrease because of an increase in the charge carrier density, weakening the electrostatic attraction of the dopant defects to the surface. We demonstrated direct evidence of the chemical expansion/contraction effect on the cation segregation, using the lattice parameters deduced from high-resolution XRD patterns as a function of the oxygen pressure. We believe the chemical expansion to be the dominant factor that suppresses the segregation at the lower oxygen pressures. Segregation of Ba and Sr induced a heterogeneous structure and chemistry at the surface, in the form of dopant-oxides. Image contrast between the topography recorded by AFM and STM revealed that these surface chemical heterogeneities were electronically insulating. Such insulating secondary phases at the surface are expected to hinder the charge transfer in ORR on the cathode surface.

We believe that the mechanisms that we identified to govern the cation segregation on the doped $LnMnO_3$ films are actually applicable to a wider family of perovskite oxide surfaces. Both the elastic and electrostatic interactions must be quantitatively taken into account in assessing the surface segregation of cations on this fascinatingly complex and technologically important family of materials. Systematic investigation of chemical, structural, and electrical impact of dopant segregation on such systems is important for a range of applications, including oxygen permeation membranes, batteries, magnetic and ferroelectric materials as well as fuel cells. Further in-depth studies on how these cation rearrangements correlate to the electrochemical activity and stability under a broader range of conditions is essential toward advancing our predictive capabilities to design optimal SOFC cathode surfaces.

■ ASSOCIATED CONTENT

Ⓢ Supporting Information

Figure S1, chemical analysis on heterogeneous surfaces with combination of AR-XPS and AFM; Figure S2, calculation of surface segregation energy with DFT simulation; Figures S3 and S4, analysis of the high-resolution photoelectron spectra from the dopant core level emissions; Figure S5, localized chemical composition and structure on the annealed LSM films; Figure S6, schematic illustration of the local distribution of charged species at and near the surface; Figure S7, C 1s peak analysis as a function of temperature at two emission angles, Figures S8 and S9, surface structure and chemistry on LBM films upon annealing in different gas conditions; Figure S10, DFT-calculated surface segregation energies of Ca, Sr, and Ba dopant; Figure S11, surface structure of annealed LBM films images with AFM and STM; Table S1, DFT-calculated bulk (shear) modulus; and Table S2, standard enthalpies of formation for the possible secondary phases. This material is available free of charge via the Internet at http://pubs.acs.org.

■ AUTHOR INFORMATION

Corresponding Author

byildiz@mit.edu

Author Contributions

[†]These authors contributed equally.

Notes

The authors declare no competing financial interest.

■ ACKNOWLEDGMENTS

The authors gratefully acknowledge the financial support from the US-DOE - Office of Fossil Energy, grant no. DE-NT0004117 for the experimental component of this work, and Basic Energy Sciences, grant no. DE-SC0002633 for the computational component of this work; the National Science Foundation for computing support through the XSEDE Program, grant no. TG-ASC090058 and TG-DMR110004; Caroline Ross and Harry Tuller at MIT for the use of their PLD system, and Jae Jin Kim for his help on PLD target fabrication.

■ REFERENCES

(1) Cai, Z.; Kubicek, M.; Fleig, J.; Yildiz, B. *Chem. Mater.* **2012**, *24*, 1116−1127.

(2) Cai, Z.; Kuru, Y.; Han, J. W.; Chen, Y.; Yildiz, B. *J. Am. Chem. Soc.* **2011**, *133*, 17696−17704.

(3) Chen, Y.; Jung, W.; Cai, Z.; Kim, J. J.; Tuller, H. L.; Yildiz, B. *Energy Environ. Sci.* **2012**, *5*, 7979−7988.

(4) Crumlin, E. J.; Mutoro, E.; Ahn, S.-J.; la O', G. J.; Leonard, D. N.; Borisevich, A.; Biegalski, M. D.; Christen, H. M.; Shao-Horn, Y. *J. Phys. Chem. Lett.* **2010**, *1*, 3149−3155.

(5) Jiang, S. *J. Solid State Electrochem.* **2007**, *11*, 93−102.

(6) Jung, W.; Tuller, H. L. *Energy Environ. Sci.* **2012**, *5*, 5370−5378.

(7) Kubicek, M.; Limbeck, A.; Frömling, T.; Hutter, H.; Fleig, J. *J. Electrochem. Soc.* **2011**, *158*, B727−B734.

(8) Mutoro, E.; Crumlin, E. J.; Biegalski, M. D.; Christen, H. M.; Shao-Horn, Y. *Energy Environ. Sci.* **2011**, *4*, 3689−3696.

(9) Shin, T. H.; Ida, S.; Ishihara, T. *J. Am. Chem. Soc.* **2011**, *133*, 19399−19407.

(10) Tsai, C.-Y.; Dixon, A. G.; Ma, Y. H.; Moser, W. R.; Pascucci, M. R. *J. Am. Ceram. Soc.* **1998**, *81*, 1437−1444.

(11) Yang, L.; Tan, L.; Gu, X.; Jin, W.; Zhang, L.; Xu, N. *Ind. Eng. Chem. Res.* **2003**, *42*, 2299−2305.

(12) Levi, E.; Mitelman, A.; Aurbach, D.; Brunelli, M. *Chem. Mater.* **2007**, *19*, 5131−5142.

(13) Yabuuchi, N.; Lu, Y.-C.; Mansour, A. N.; Chen, S.; Shao-Horn, Y. *J. Electrochem. Soc.* **2011**, *158*, A192−A200.

(14) Yoon, W.-S.; Paik, Y.; Yang, X.-Q.; Balasubramanian, M.; McBreen, J.; Grey, C. P. *Electrochem. Solid-State Lett.* **2002**, *5*, A263−A266.

(15) Lee, S. W.; Carlton, C.; Risch, M.; Surendranath, Y.; Chen, S.; Furutsuki, S.; Yamada, A.; Nocera, D. G.; Shao-Horn, Y. *J. Am. Chem. Soc.* **2012**, *134*, 16959−16962.

(16) Serrate, D.; De Teresa, J. M.; Blasco, J.; Ibarra, M. R.; Morellon, L.; Ritter, C. *Appl. Phys. Lett.* **2002**, *80*, 4573−4575.

(17) Rao, C. N. R.; Vanitha, P. V. *Curr. Opin. Solid State Mater. Sci.* **2002**, *6*, 97−106.

(18) Estrade, S.; Arbiol, J.; Peiro, F.; Infante, I. C.; Sanchez, F.; Fontcuberta, J.; de la Pena, F.; Walls, M.; Colliex, C. *Appl. Phys. Lett.* **2008**, *93*, 112505−3.

(19) Estrade, S.; Rebled, J. M.; Arbiol, J.; Peiro, F.; Infante, I. C.; Herranz, G.; Sanchez, F.; Fontcuberta, J.; Cordoba, R.; Mendis, B. G.; Bleloch, A. L. *Appl. Phys. Lett.* **2009**, *95*, 072507−3.

(20) Hamada, I.; Uozumi, A.; Morikawa, Y.; Yanase, A.; Katayama-Yoshida, H. *J. Am. Chem. Soc.* **2011**, *133*, 18506−18509.

(21) Stavale, F.; Shao, X.; Nilius, N.; Freund, H.-J.; Prada, S.; Giordano, L.; Pacchioni, G. *J. Am. Chem. Soc.* **2012**, *134*, 11380−11383.

(22) Arredondo, M.; Ramasse, Q. M.; Weyland, M.; Mahjoub, R.; Vrejoiu, I.; Hesse, D.; Browning, N. D.; Alexe, M.; Munroe, P.; Nagarajan, V. *Adv. Mater.* **2010**, *22*, 2430−2434.

(23) Miles, G. C.; Stennett, M. C.; Reaney, I. M.; West, A. R. *J. Mater. Chem.* **2005**, *15*, 798−802.

(24) Jiang, S. P. *J. Solid State Electrochem.* **2005**, *11*, 93−102.

(25) la O, G. J.; Ahn, S.-J.; Crumlin, E.; Orikasa, Y.; Biegalski, M. D.; Christen, H. M.; Shao-Horn, Y. *Angew. Chem., Int. Ed.* **2010**, *49*, 5344−5347.

(26) Brandon, N. P.; Skinner, S.; Steele, B. C. H. *Ann. Rev. Mater. Res.* **2003**, *33*, 183−213.

(27) Chueh, W. C.; Haile, S. M. *Annu. Rev. Chem. Bio. Eng.* **2012**, *3*, 313−341.

(28) Adler, S. B. *Chem. Rev.* **2004**, *104*, 4791−4844.

(29) Shao, Z.; Haile, S. M. *Nature* **2004**, *431*, 170−173.

(30) Jalili, H.; Han, J. W.; Kuru, Y.; Cai, Z.; Yildiz, B. *J. Phys. Chem. Lett.* **2011**, *2*, 801−807.

(31) Fister, T. T.; Fong, D. D.; Eastman, J. A.; Baldo, P. M.; Highland, M. J.; Fuoss, P. H.; Balasubramaniam, K. R.; Meador, J. C.; Salvador, P. A. *Appl. Phys. Lett.* **2008**, *93*, 151904−3.

(32) Dulli, H.; Dowben, P. A.; Liou, S. H.; Plummer, E. W. *Phys. Rev. B* **2000**, *62*, R14629−R14632.

(33) Katsiev, K.; Yildiz, B.; Balasubramaniam, K.; Salvador, P. A. *Appl. Phys. Lett.* **2009**, *95*, 092106−3.

(34) Wang, W.; Jiang, S. P. *Solid State Ionics* **2006**, *177*, 1361−1369.

(35) Szot, K.; Speier, W. *Phys. Rev. B* **1999**, *60*, 5909−5926.

(36) Liang, Y.; Bonnell, D. A. *Surf. Sci.* **1994**, *310*, 128−134.

(37) Han, J. W.; Kitchin, J. R.; Sholl, D. S. *J. Chem. Phys.* **2009**, *130*, 124710−8.

(38) Lussier, A.; Dvorak, J.; Stadler, S.; Holroyd, J.; Liberati, M.; Arenholz, E.; Ogale, S. B.; Wu, T.; Venkatesan, T.; Idzerda, Y. U. *Thin Solid Films* **2008**, *516*, 880−884.

(39) Lee, J.-R.; Chiang, Y.-M. *Solid State Ionics* **1995**, *75*, 79−88.

(40) Battaile, C. C.; Najafabadi, R.; Srolovitz, D. J. *J. Am. Ceram. Soc.* **1995**, *78*, 3195−3200.

(41) Wynblatt, P.; Rohrer, G. S.; Papillon, F. *J. Eur. Ceram. Soc.* **2003**, *23*, 2841−2848.

(42) Guo, X. *Solid State Ionics* **1995**, *81*, 235−242.

(43) Cockroft, N. J.; Lee, S. H.; Wright, J. C. *Phys. Rev. B* **1991**, *44*, 4117−4126.

(44) Lee, H. B.; Prinz, F. B.; Cai, W. *Acta Mater.* **2010**, *58*, 2197−2206.

(45) van der Heide, P. A. W.; Rabalais, J. W. *Chem. Phys. Lett.* **1998**, *297*, 350−356.

(46) Lee, W.; Jung, H. J.; Lee, M. H.; Kim, Y.-B.; Park, J. S.; Sinclair, R.; Prinz, F. B. *Adv. Funct. Mater.* **2012**, *22*, 965−971.

(47) Estrade, S.; Arbiol, J.; Peiro, F.; Abad, L.; Laukhin, V.; Balcells, L.; Martinez, B. *Appl. Phys. Lett.* **2007**, *91*, 252503−3.

(48) Kilner, J. A. *Chem. Lett.* **2008**, *37*, 1012−1015.

(49) Harrison, W. A. *Phys. Rev. B* **2011**, *83*, 155437.

(50) Horvath, G.; Gerblinger, J.; Meixner, H.; Giber, J. *Sens. Actuators, B* **1996**, *32*, 93−99.

(51) Martin, M. *J. Kor. Ceram. Soc.* **2012**, *49*, 29−36.

(52) Shannon, R. *Acta Crystallogr., Sect. A* **1976**, *32*, 751−767.

(53) D'Souza, C. M.; Sammes, N. M. *J. Am. Ceram. Soc.* **2000**, *83*, 47−52.

(54) *NIST Database 82*; U.S. Department of Commerce: Washington, DC, 2001, accessed in 2011/2012.

(55) Kresse, G.; Furthmüller, J. *Phys. Rev. B* **1996**, *54*, 11169−11186.

(56) Perdew, J. P.; Chevary, J. A.; Vosko, S. H.; Jackson, K. A.; Pederson, M. R.; Singh, D. J.; Fiolhais, C. *Phys. Rev. B* **1992**, *46*, 6671−6687.

(57) Blöchl, P. E. *Phys. Rev. B* **1994**, *50*, 17953.

(58) Dudarev, S. L.; Botton, G. A.; Savrasov, S. Y.; Humphreys, C. J.; Sutton, A. P. *Phys. Rev. B* **1998**, *57*, 1505.

(59) Wang, L.; Maxisch, T.; Ceder, G. *Phys. Rev. B* **2006**, *73*, 195107.

(60) Han, J. W.; Jalili, H.; Kuru, Y.; Cai, Z.; Yildiz, B. *ECS Trans.* **2011**, *35*, 2097−2104.

(61) Friedel, J. *Adv. Phys.* **1954**, *3*, 446−507.

(62) Le Page, Y.; Saxe, P. *Phys. Rev. B* **2002**, *65*, 104104.

(63) Lee, Y.-L.; Morgan, D. *ECS Trans.* **2009**, *25*, 2769−2774.

(64) Kuru, Y.; Marrocchelli, D.; Bishop, S. R.; Chen, D.; Yildiz, B.; Tuller, H. L. *J. Electrochem. Soc.* **2012**, *159*, F799−F803.

(65) Kushima, A.; Yip, S.; Yildiz, B. *Phys. Rev. B* **2010**, *82*, 115435.

(66) De Souza, R. A.; Martin, M. *Phys. Chem. Chem. Phys.* **2008**, *10*, 2356−2367.

(67) Wang, R.-V.; McIntyre, P. C. *J. Appl. Phys.* **2005**, *97*, 023508−8.

(68) Lu, H.; George, T. A.; Wang, Y.; Ketsman, I.; Burton, J. D.; Bark, C. W.; Ryu, S.; Kim, D. J.; Wang, J.; Binek, C.; Dowben, P. A.; Sokolov, A.; Eom, C. B.; Tsymbal, E. Y.; Gruverman, A. *Appl. Phys. Lett.* **2012**, *100*, 232904−5.

(69) Picozzi, S.; Ma, C.; Yang, Z.; Bertacco, R.; Cantoni, M.; Cattoni, A.; Petti, D.; Brivio, S.; Ciccacci, F. *Phys. Rev. B* **2007**, *75*, 094418.

(70) Islam, M. S.; Cherry, M.; Catlow, C. R. A. *J. Solid State Chem.* **1996**, *124*, 230−237.

(71) Kovaleva, N.; Gavartin, J.; Shluger, A.; Boris, A.; Stoneham, A. *J. Exp. Theor. Phys.* **2002**, *94*, 178−190.

(72) Onufriev, A. *The generalized Born model: its foundation, applications, and limitations*U.S. DOE: Washington, DC2010, http://www.osti.gov/eprints/topicpages/documents/record/705/1923591.html, accessed in 2013.

(73) Mizusaki, J.; Mima, Y.; Yamauchi, S.; Fueki, K.; Tagawa, H. *J. Solid State Chem.* **1989**, *80*, 102−111.

(74) Mizusaki, J.; Mori, N.; Takai, H.; Yonemura, Y.; Minamiue, H.; Tagawa, H.; Dokiya, M.; Inaba, H.; Naraya, K.; Sasamoto, T.; Hashimoto, T. *Solid State Ionics* **2000**, *129*, 163−177.

(75) Liu, Z.; Cheng, L.-Z.; Han, M.-F. *J. Power Sources* **2011**, *196*, 868−871.

(76) Konysheva, E. Y.; Xu, X.; Irvine, J. T. S. *Adv. Mater.* **2012**, *24*, 528−532.

(77) Poulsen, F. W. *Solid State Ionics* **2000**, *129*, 145−162.

(78) Murugavel, P.; Lee, J. H.; Lee, K.-B.; Park, J. H.; Chung, J.-S.; Yoon, J.-G.; Noh, T. W. *J. Phys. D: Appl. Phys.* **2002**, *35*, 3166−3170.

(79) Kathrin, D. *J. Phys. D: Appl. Phys.* **2006**, *39*, R125.

(80) Haghiri-Gosnet, A. M.; Renard, J. P. *J. Phys. D: Appl. Phys.* **2003**, *36*, R127.

(81) Marrocchelli, D.; Bishop, S. R.; Tuller, H. L.; Yildiz, B. *Adv. Func. Mater.* **2012**, *22*, 1958−1965.

(82) Marrocchelli, D.; Bishop, S. R.; Tuller, H. L.; Watson, G. W.; Yildiz, B. *Phys. Chem. Chem. Phys.* **2012**, *14*, 12070−12074.

(83) Wu, W.; Wong, K. H.; Mak, C. L.; Choy, C. L.; Zhang, Y. H. *J. Appl. Phys.* **2000**, *88*, 2068−2071.

(84) Ogale, A. S.; Shinde, S. R.; Kulkarni, V. N.; Higgins, J.; Choudhary, R. J.; Kundaliya, D. C.; Polleto, T.; Ogale, S. B.; Greene, R. L.; Venkatesan, T. *Phys. Rev. B* **2004**, *69*, 235101.

(85) Yin, Z.; Gao, G.; Huang, Z.; Jiao, X.; Liu, Q.; Wu, W. *J. Phys. D: Appl. Phys.* **2009**, *42*, 125002.

(86) Oh, D.; Gostovic, D.; Wachsman, E. D. *J. Mater. Res.* **2012**, *27*, 1992−1999.

(87) Huber, A.-K.; Falk, M.; Rohnke, M.; Luerßen, B.; Gregoratti, L.; Amati, M.; Janek, J. *Phys. Chem. Chem. Phys.* **2012**, *14*, 751−758.

(88) Ju, H. L.; Gopalakrishnan, J.; Peng, J. L.; Li, Q.; Xiong, G. C.; Venkatesan, T.; Greene, R. L. *Phys. Rev. B* **1995**, *51*, 6143−6146.

(89) Seo, S. H.; Kang, H. C.; Jang, H. W.; Noh, D. Y. *Phys. Rev. B* **2005**, *71*, 012412.

(90) Goyal, A.; Rajeswari, M.; Shreekala, R.; Lofland, S. E.; Bhagat, S. M.; Boettcher, T.; Kwon, C.; Ramesh, R.; Venkatesan, T. *Appl. Phys. Lett.* **1997**, *71*, 2535−2537.

(91) Salvato, M.; Vecchione, A.; De Santis, A.; Bobba, F.; Cucolo, A. M. *J. Appl. Phys.* **2005**, *97*, 103712−5.

(92) Watts, B. E.; Leccabue, F.; Tallarida, G.; Ferrari, S.; Fanciulli, M.; Padeletti, G. *J. Electroceram.* **2003**, *11*, 139−147.

(93) Watts, B. E. *Process. Appl. Ceram.* **2009**, *3*, 97−101.

(94) Hwang, H. Y.; Iwasa, Y.; Kawasaki, M.; Keimer, B.; Nagaosa, N.; Tokura, Y. *Nat. Mater.* **2012**, *11*, 103−113.

(95) Petrov, A. N.; Kononchuk, O. F.; Andreev, A. V.; Cherepanov, V. A.; Kofstad, P. *Solid State Ionics* **1995**, *80*, 189−199.

(96) Kawada, T.; Yokokawa, H. *Key Eng. Mater.* **1997**, *125−126*, 187−248.

(97) Jacobson, A. J. *Chem. Mater.* **2010**, *22*, 660−674.

(98) Orlovskaya, N.; Kleveland, K.; Grande, T.; Einarsrud, M.-A. *J. Eur. Ceram. Soc.* **2000**, *20*, 51−56.

(99) Rajendran, V.; Muthu Kumaran, S.; Sivasubramanian, V.; Jayakumar, T.; Raj, B. *Phys. Status Solidi A* **2003**, *195*, 350−358.

(100) Lee, Y.-L.; Kleis, J.; Rossmeisl, J.; Morgan, D. *Phys. Rev. B* **2009**, *80*, 224101.

(101) Islam, M. S. *J. Mater. Chem.* **2000**, *10*, 1027−1038.

(102) Khan, M. S.; Islam, M. S.; Bates, D. R. *J. Phys. Chem. B* **1998**, *102*, 3099−3104.

(103) De Souza, R. A.; Maier, J. *Phys. Chem. Chem. Phys.* **2003**, *5*, 740−748.

(104) Jones, A.; Islam, M. S. *J. Phys. Chem. C* **2008**, *112*, 4455−4462.

(105) Akashi, T.; Nanko, M.; Maruyama, T.; Shiraishi, Y.; Tanabe, J. *J. Electrochem. Soc.* **1998**, *145*, 2090−2094.

(106) Smith, J. B.; Norby, T. *Solid State Ionics* **2006**, *177*, 639−646.

(107) Horita, T.; Ishikawa, M.; Yamaji, K.; Sakai, N.; Yokokawa, H.; Dokiya, M. *Solid State Ionics* **1998**, *108*, 383−390.

(108) Horita, T.; Ishikawa, M.; Yamaji, K.; Sakai, N.; Yokokawa, H.; Dokiya, M. *Solid State Ionics* **1999**, *124*, 301−307.

(109) Kuru, Y.; Jalili, H.; Cai, Z.; Yildiz, B.; Tuller, H. L. *Adv. Mater.* **2011**, *23*, 4543−4548.

(110) Labidi, M.; Labidi, S.; Ghemid, S.; Meradji, H.; Hassan, F. E. H. *Phys. Scr.* **2010**, *82*, 045605.

(111) Jiang, S. *J. Solid State Electrochem.* **2007**, *11*, 93−102.

(112) Simner, S. P.; Anderson, M. D.; Engelhard, M. H.; Stevenson, J. W. *Electrochem. Solid-State Lett.* **2006**, *9*, A478−A481.